FABRICATION AND CHARACTERIZATION OF PCL-nHA COMPOSITE SCAFFOLDS BY USING NON-SOLVENT INDUCED PHASE SEPARATION TECHNIQUE IN BONE TISSUE ENGINEERING

Mehmet Serhat Aydın

Submitted to the Graduate School of Engineering and Natural Sciencs
In partial fulfillment of the requirements for the degree of
Master of Science

Sabanci University
August 2019

TITLE OF THE THESIS

FABRICATION AND CHARACTERIZATION OF PCL-nHA COMPOSITE SCAFFOLDS WITH MULTI SCALE POROSITY USING NON-SOLVENT INDUCED PHASE SEPARATION TECHNIQUE IN BONE TISSUE ENGINEERING

APPROVED BY:

Assoc. Prof. Güllü Kızıltaş Şendur .....
(Thesis Supervisor)

Assoc. Prof. Gözde Özaydın İnce.....

Assoc. Prof. Çetin Yılmaz .....

DATE OF APPROVAL: 19.07.2019

FABRICATION AND CHARACTERIZATION OF PCL-nHA COMPOSITE SCAFFOLDS BY USING NON-SOLVENT INDUCED PHASE SEPARATION TECHNIQUE IN BONE TISSUE ENGINEERING

Mehmet Serhat Aydın

Master of Science Thesis, 2019

Supervisor: Assoc. Prof. Gullu Kiziltas Sendur

Keywords: Bone Tissue Engineering, Non-solvent Induced Phase Separation, PCL-nHA scaffolds, Coating via ICVD.

Abstract

Bone fracture, one of the widespread injuries all around the world, is associated with individual disability and loss of social productivity resulting in very high treatment costs exceeding billion dollars. Well-designed scaffold implants are good alternatives in bone tissue engineering known to result in effective healing. An ideal bone scaffold should be biocompatible, porous, interconnected and strong, i.e. multi-functional. Therefore, composite materials with multi-scale porosities stand out as key desired scaffold features. Solid free-form fabrication (SFF) techniques exist with mechanical and biological functions tailorable to specific bone defects. However, only a few attempts have been made to create scaffolds with macro-micro porosity, despite their potential to more closely mimic the hierarchical architecture of native bones. Non-solvent induced phase separation technique (NIPS), mostly used in literature for the fabrication of membranes, is an effective technique capable to produce scaffolds with desired tunable porosities at different scales and offers the potential to be integrated to 3D printing. Towards that goal, this thesis focuses on an in-depth study of the pore morphology and its dependence on the composition of porous poly(ε-caprolactone) (PCL)/hydroxyapatite (HA) composites substrates at various thicknesses using the NIPS process. More specifically, the aim of this study is to fabricate and characterize PCL-nHA composite porous scaffolds having various nHA content (0, 10, 20% w/w) and thicknesses (800-900 and 1600-1800 microns) based on NIPS and understand its potential to produce 3D scaffolds when integrated to 3D printing. Effect of PCL concentration, nHA content and scaffold thickness were investigated on scaffold porosity and morphology such as pore size and its distribution, pore orientation and overall porosity. Internal micro-structure of the substrates are analyzed by micro-CT and SEM analysis was used for surface porosity analysis and validation of micro-CT results. Pore size distrubution, overall porosity and anistropy of pore network were evaluated based on micro-CT images and CTAnalyzer software. Rheological anlysis and UTM tests were also performed to analyze the solution's viscosity and resulting composite's strength. Atomic composition evaluation of scaffolds was conducted with EDS. Bone mineral density -for the detection of amount of Hydroxyapatite- measurement was computed by micro-CT. In addition to analysis of film scaffolds, the NIPS process is used to produce 2D layers of interconnected scaffolds using

a commercial bioprinter as an initial step towards its use for the production of 3D scaffolds with controlled macro-porosity. Our results demonstrated that scaffold thickness and addition of nHA both enhance pore diameter in size. Micro-CT and SEM analyses showed that PCL-nHA scaffolds with various nHA content have multiscale porosities in micro (<50 microns) and macro (>50 microns) scale. While increase of thickness enhances pore size, increase of PCL concentration decreases pore size and overall porosity. Addition of nHA is linked to higher strength and lower viscosity upto a threshold value whereas leading to overall porosity, larger pore size, higher pore network orientation (anisotropy). SEM images confirm the pore size distribution result obtained by micro CT at the cross section and inhomogeneous porosity at the surface as well as a more homogeneous porosity distribution in the cross sections of both film scaffolds and the printed 2D grid scaffold. For surface functionalization, the scaffolds were coated with p(HEMA-*co*-EGDMA) via iCVD to increase surface hydrophilicity which is known to improve cell adhesion. Result of FTIR, and ellipsometer demonstrated that scaffold surface was coated successfully, and contact angle measurement showed that a hydrophilic surface was obtained. This thesis has demonstrated that NIPS can be integrated to 3D printing and successfully produce scaffolds with well controlled macro-pores and tunable micro-pores.

KEMİK DOKUSU MÜHENDİSLİĞİNDE SOLVENT OLMAYAN İNDÜKLENMİŞ FAZ AYIRMA TEKNİĞİ KULLANARAK PCL-nHA KOMPOZİT İSKELEME FABRİKASYONU VE KARAKTERİZASYONU

Mehmet Serhat Aydın

Yüksek Lisans Tezi, 2019

Tez Danışmanı: Doç. Dr. Güllü Kızıltaş Şendur

Keywords: Kemik Doku Mühendisliği, Solvent Olmayan İndüklenmiş Faz Ayırma Tekniği, PCL-nHA iskeleleri, iCVD ile kaplama

Özet

Dünya genelinde gerçekleşen yaygın yaralanmalardan biri olan kemik kırığı sakatlık ve sosyal üretkenlik kaybı ile ilişkili olup tedavi maliyetleri milyar doları aşmaktadır. İyi tasarlanmış doku iskele implantları, etkili iyileşme ile sonuçlandığı bilinen kemik dokusu mühendisliğinde etkili olmaktadır. İdeal bir kemik iskelesi biyolojik olarak uyumlu, gözenekli ve gözeneklerin birbirine bağlı olduğu bir yapıda çok işlevli olmalıdır. Bu nedenle, çok ölçekli gözeneklere sahip olan kompozit malzemeler istenen iskele özellikleri olarak öne çıkmaktadır. Katı serbest formlu imalat (SFF) teknikleri, spesifik kemik kusurlarına atfedilebilen mekanik ve biyolojik fonksiyonlarla mevcuttur. Bununla birlikte, doğal kemiklerin hiyerarşik yapısını daha fazla taklit etme potansiyellerine rağmen, literatürde makro-mikro gözenekli iskeleler oluşturmak için yeterli sayıda çalışma mevcut değildir. Çoğunlukla membranların imalatı için literatürde kullanılan, çözücü olmayan kaynaklı faz ayırma tekniği (NIPS), farklı ölçeklerde istenen ayarlanabilir gözeneklere sahip iskeleler üretebilen ve 3D baskıya entegre olma potansiyeli olan etkili bir tekniktir. Bu amaca yönelik olarak, bu tez gözenek morfolojisinin derinlemesine bir incelemesine ve bunun gözenekli poli (ε-kaprolakton) (PCL) / hidroksiapatit (HA) bileşiklerinin NIPS işlemini kullanarak çeşitli kalınlıklardaki bileşimine bağımlılığına odaklanmaktadır. Daha spesifik olarak, bu çalışmanın amacı, NIPS'e dayanan çeşitli nHA içeriğine (ağırlıkça% 0, 10,% 20) ve kalınlığa (800-900 ve 1600-1800 mikron) sahip PCL-nHA kompozit gözenekli iskeleleri üretmek ve karakterize etmektir. Bunlara ek olarak, bu tez kapsamında, bu metot sonucu elde edilen solüsyonun 3D baskıya entegre edildiğinde 3D iskeleler üretme potansiyelinin anlaşılması amaçlanmıştır. PCL konsantrasyonunun, nHA içeriğinin ve iskele kalınlığının iskele gözenekliliği ve iskelenin morfolojik özelliklerine (gözenek büyüklüğü ve dağılımı, gözenek yönü ve genel gözeneklilik) etkileri incelenmiştir. Üretilen substratların iç mikro yapısı mikro-CT ile analiz edilmiş ve yüzey-porozite analizi ve mikro-CT sonuçlarının doğrulanması için SEM analizi kullanılmıştır. Gözenek büyüklüğünün dağılması, genel gözeneklilik ve gözeneklerin yöne bağımlılığı, mikro-CT görüntüleri ve CTAnalyzer yazılımı kullanılarak değerlendirildi. Çözümün viskozitesini ve sonuçta ortaya çıkan kompozitin gücünü analiz etmek için reolojik analiz ve UTM testleri de yapıldı. Yapı iskelelerinin atomik kompozisyon değerlendirmesi EDS ile yapılmıştır. Kemik mineral yoğunluğu (Hidroksiapatit miktarının tespiti) ölçümü, mikro-CT ile hesaplandı. Film yapı iskelelerinin analizine ek olarak, NIPS işlemi, kontrollü

makro gözenekliliğe sahip 3D yapı iskelelerinin üretimi için kullanımına yönelik ilk adım olarak ticari bir bioprinter kullanan bir 2D bağlantı birbirine bağlanmış yapı iskelesi katmanları üretmek için kullanılmıştır. Elde edilen sonuçlar iskele kalınlığının ve nHA ilavesinin hem gözenek çapını arttırdığını göstermiştir. Micro-CT ve SEM analizleri, çeşitli nHA içeriğine sahip PCL-nHA yapı iskelelerinin mikro (<50 mikron) ve makro (> 50 mikron) ölçeğinde çok ölçekli gözeneklere sahip olduğunu göstermiştir. Ayrıca, kalınlık artışının gözenek boyutunu arttırdığı, PCL konsantrasyonunun artışının gözenek boyutunu ve genel gözenekliliği azalttığı görülmüştür. nHA ilavesi, genel gözeneklilik, daha büyük gözenek boyutu, daha yüksek gözenek ağının oryantasyonuna (anizotropi) yol açan eşik değere kadar daha yüksek mukavemet ve daha düşük viskozite ile bağlantılıdır. SEM görüntüleri, kesitte mikro CT tarafından elde edilen ve yüzeyde homojen olmayan bir gözeneklilik ve hem film yapıların hem de 2D ızgara iskelenin kesitlerinde daha homojen bir gözeneklilik dağılımı sergileyen gözenek büyüklüğü dağılım sonucunu teyit etmektedir. Tezin ikinci kısmında, yüzey modifikasyonlarının yapılması için iskeleler yüzey hidrofilisitesini arttırmak için iCVD yoluyla hücre tutunumuna yardımcı olduğu bilinen p (HEMA-ko-EGDMA) ile kaplandı. FTIR ve elipsometre sonuçları, iskele yüzeyinin başarıyla kaplandığını ve temas açısı ölçümü de hidrofilik yüzeyin elde edildiğini göstermiştir.

To my people…

Table of Contents

List of Figures

List of Tables

List of Abbreviations

HA	Hydroxyapatite
PGA	Polyglycolide
PLA	Polylactic acid
PCL	Polycaprolactone
PLGA	Poly(lactic-*co*-glycolic acid)
NIPS	Non-solvent Induced Phase Separation
WNM	Wired Network Modelling
SFF	Solid Free Form
FDM	Fused Deposition Modeling
p(HEMA)	Poly(2-hydroxyethyl methacrylate)
EGDMA	Ethylene glycol dimethacrylate
SEM	Scanning Electron Microscopy
Micro-CT	Micro Computational Tomogaphy
UTM	Universal Testing Machine
iCVD	Initiated Chemical Vapor Deposition
FTIR	Fourier-transform infrared spectroscopy
EDS	Energy-dispersive X-ray spectroscopy
µ, um	Microns

Acknowledgement

First of all, I would like to thank my thesis supervisor Assoc. Prof. Güllü Kızıltaş Şendur for her support, guidance and advices throughout my master studies. I am appreciated to Assoc. Prof. Gözde İnce and her research group members for collabration with my research. I would like to thank my thesis jury members Assoc. Prof. Gözde İnce and Assoc. Prof. Çetin Yılmaz for their precious comments and contributions.

I am also grateful to Dr. Ali Tufani, Dr. Onur Zihni Çalışkan; grad students Sepideh Shemshad, Semih Pehlivan, Mervenaz Şahin, Can Akaoğlu, Barış Emre Kıral; technical personal Nursel Karakaya for helping me during characterization process. Also, co-space workers Çağdaş Erk and Zafer Çömlekçi for their warm welcome.

I would like to thank my collegues Ogeday Rodop, Elif Çelik, Dilara Kaya, Caner Dikyol, Adnan Taşdemir, and Ebru Çetin for their support.

I want to thank Sezin Sayın with all my heart. She understands me all the time, made me peaceful and who was there for me whenever I need.

Lastly, I want to thank my family for their continuous encouragement, support, patience and love. Wherever I go, they were and will always with me. Therefore, I would like to dedicate my thesis study to my family and my people.

Chapter 1

Introduction

1.1. Motivation

Bone fracture, one of the widespread injuries all around the world, is associated with individual disability and loss of social productivity resulting in very high treatment costs exceeding billion dollars [1]. Well-designed scaffold implants are good alternatives in bone tissue engineering known to result in effective healing.

Bone is a natural composite material consisting mostly of hydroxyapatite (HA) which is a ceramic based on calcium as well as phosphate, proteins and other inorganic compounds. Therefore, like an original bone, an ideal bone scaffold needs to be biocompatible. Biopolymers especially thermoplastics such as polyglycolide (PGA), polylactic acid (PLA), polycaprolactone (PCL), poly(lactic-*co*-glycolic acid) (PLGA) are very popular thanks to their compatibility with living body and their ability to degrade in time providing a temporary artificial medium for the bone healing processes until the formation of new bone tissue [2].

Besides biocompatibility, an ideal scaffold should be porous for migration and proliferation of mesenchymal cells and formation of vascular and angiogenetic network within tissue [3]. Bone itself has a porous structure to allow molecular transportation and transmission. Consequently, an ideal scaffold needs enough porosity with pore size ranging between approximately 100 microns and 300 microns in size for cell migration and delivery of molecules through the material. In addition, pores greater than 300 microns in size are needed for vascularization, angiogenesis and new bone formation [4]. However, fibrous tissue can form and penetrate even in smaller pores between 10 microns to 75 microns in size [5]. Therefore, fabricated scaffolds, among others, for effective bone

healing must meet pore size requirements that will be referred to as multi-scale or macro-micro porosity in this thesis.

Porosity and pore size directly affect scaffolds' surface properties altering its biological and mechanical functions. For instance, micropores (< 50 microns) cause larger surface area and may result in higher surface roughness changing the surface hydrophilicity or hydrophobicity through a change in contact angle [6] and resulting in an increase of cell attachment, cell proliferation and cell differentiation [7].

Similar to porosity and pore size, the interconnected geometry of the scaffold is desired with a uniformly distributed porosity enhancing cell seeding and materials strength [8] [9]. Therefore, porous scaffold should retain an interconnected network as well.

In literature, various techniques are presented attempting to produce porous scaffolds with porosities at different scales to improve biological activities and healing in bone tissue engineering. Among these, polymer impregnation [10] and hybrid methods such as solvent casting & particulate leaching [11], gas foaming & salt leaching [12], wired network modelling (WNM) [13], [14], [15] and electrospinning [16], [17], [18] as well as various forms of solid free form fabrication techniques (SFF) [19], [20], [21], [22] stand out. However, each technique has its own advantages and disadvantages. And as discussed in more detail in the literature review chapter, most of these techniques are time consuming and post processing, require specialized equipment or are based on solvents. Therefore, they are not readily suitable for integration to 3D printing and do not allow for the formation of well distributed pores and reproduction of porous scaffolds.

Among these fabrication techniques, a more recent technique known as non-solvent induced phase separation (NIPS) is known to be advantageous in terms of obtaining desired multi scale porosity mostly used for the production of membranes [23], [24], [25]. This is the main method chosen in the production of scaffolds of well-distributed micro-pores.

Integration of NIPS technique with 3D printing towards producing scaffolds with controlled macro pores in addition to micro-pores was studied by Kim et al. [26] to fabricate a PCL-HA scaffold demonstrating its capability to induce micro-pores to the scaffolds. However, as discussed in detail in the literature review chapter, their study did not examine the effects of thickness and PCL concentration on PCL-HA scaffolds nor the

internal porous microstructure morphology such as pore orientation and pore size distribution affecting the bone regeneration process and hence effective bone healing.

1.1. Objective

The major goal of this study is to fill the aforementioned gaps in literature and explore the potential of NIPS integrated to 3D printing in detail towards the production of substrates with controlled and tunable multi-scale porosities and thicknesses suitable for the production of various 3D scaffolds. Towards that goal, in this thesis we present an in-depth study of the pore morphology and its dependence on process parameters in PCL-HA composites with varying thicknesses that are produced using the NIPS process. We would like to study the effect of nHA content, PCL concentration and scaffold thickness on the structure of pore, pore size distribution, overall porosity and pore anisotropy of the PCL-nHA scaffolds using NIPS. The major goal is to show that the NIPS integrated 3D printing is a feasible technique to produce composite scaffolds with desired morphology and tunable micro-macro porosities. Towards the major objective, a more specific objective is to address the existence of pores on the surface of the produced scaffolds. We would like to answer and fill the gap about the existence and characteristics of the surface porosity motivated by the conflicting views in literature about surface porosity of the PCL-HA scaffolds produced using NIPS. Study of Sohn et al. [15] claims that the surface porosity only exist if the mold for casting of NIPS slurry is covered, but surface pores do not exist in an uncovered mold in contrary to the study by Kim et al. [26].

1.2. Contributions

Most of the existing SFF based fabrication techniques in literature are time consuming and cost ineffective, require specialized equipment or are based on solvents. Therefore, they are not readily suitable for integration to 3D printing and do not allow for the formation of well distributed pores and reproduction of porous scaffolds. There are very few studies on the use of NIPS towards the 3D fabrication of scaffolds which has the potential of fulfilling this gap and is the main focus of this thesis. Although Kim et al. [26] is the only study to our knowledge using NIPS with 3D printing to produce PCL-HA scaffold, in their study, pores were only shown to exist internally throughout the cross section of produced macro struts but not on the surface of struts. Moreover, the effect on the scaffold's morphology of PCL, nHA content and thickness missing. Additionally, as discussed in the previous section, conflicting observations are made in literature about

the existence of surface pores. As a result of the in-depth characterization of the scaffold porosities using Micro-CT and SEM, we aim to shed light on the existing dilemma by analyzing both internal and outer surface porosities of films and scaffolds produced using NIPS integrated to a commercial printer.

When compared with studies producing films using NIPS very few studies exist analyzing the effects of porosity in thick substrates but mostly use NIPS or its variation in thin substrates or membranes. Therefore, this is the initial attempt to investigate the fabrication possibility of thick substrates with multi-scale porosity using PCL-HA materials and its in-depth analysis of the internal pore morphology using micro-CT analysis where most of the studies are rather using SEM i.e. characterization of specific cross sections.

When compared with studies producing films using NIPS very few studies exist analyzing the effects of porosity in thick substrates rather than in membranes. Additionally, this is the initial attempt to investigate the fabrication possibility of thick substrates with multi-scale porosity using PCL-HA and its in-depth analysis of the internal pore morphology using micro-CT where most of the studies are using SEM characterization.

The add-on study of PCL-nHA samples fabricated by NIPS that were coated with poly(2-hydroxyethyl methacrylate-*co*-ethylene glycol dimethacrylate) (p(HEMA-*co*-EGDMA)) via initiated chemical vapor deposition (iCVD) towards obtaining hydrophilic surfaces are known to increase cell adhesion/attachment through increase of hydrophilicity but were not presented for iCVD coated scaffolds produced using NIPS. It is possible to coat PCL polymers via iCVD and the studies have shown that both p(HEMA) and p(HEMA-*co*-EDGMA) are biocompatible polymers. In the scope of this study, we will try to demonstrate hydrophilic and insoluble surface properties on PCL-nHA scaffolds using hydrogel p(HEMA) and a crosslinker EGDMA via iCVD. Contact angle measurements will be performed to show the surface properties of coated samples. FTIR results and ellipsometer measurement will be utilized to prove the successful deposition. To the best of our knowledge iCVD coated scaffolds which were produced using NIPS do not exist.

In short, the contributions of this thesis are summarized as follows:

1. Fabrication of PCL-nHA composite substrates with multi-scale porosity and various thickness using NIPS integrated to 3D printing

2. In-depth characterization of both outer surface and internal pore morphology and distribution of NIPS films and scaffolds using micro-CT.
3. Analysis of PCL and HA content on the pore morphology, distribution, strength and viscosity within films of various thicknesses.
4. Surface coating of PCL/nHA composite thick films using iCVD.

Chapter 2

Literature Review

In this chapter, some fabrication methods that exist in literature and are shown to be capable of producing composite bone scaffolds with macro-micro porosities and interconnectivity are reviewed shortly. It is noted that only methods fabricating PCL-HA composite scaffolds with features similar to NIPS are selected with few key studies in literature using these methods are summarized. The aim of all the methods listed below in this thesis are trying to enhance PCL-HA scaffolds' performance in terms of morphological, mechanical and biological aspects.

2.1. Fabrication Methods

2.1.1. Polymer Impregnation Method

There are many fabrication techniques trying to produce well-designed multifunctional bone scaffold. The advantages of the polymer impregnation techniques are providing porous structure in 3D and similarity of interconnectivity between scaffold and trabecular bone. On the other hand, getting porosity in this way reduces the mechanical performance of the scaffold. And there will be trade-off between mechanical strength and porosity to optimize. To avoid of scarifying from either property, polymer impregnation method has been developed. In this method, by coating HA scaffold with PCL polymer lining enhances mechanical performance and strength of scaffolds still having higher interconnected porosity. In the research of Zhao et al. [10], the composite porous PCL/HA scaffold was successfully obtained by the method of polymer impregnation. The method has been indicated briefly in the paper is that, after dissolving PVA in distilled water HA powders were added to PVA solution and well mixed to get well-dispersed slurry. Subsequently, the PU foams is immersed in the HA slurry more than once in order to obtain well coated struts of the foams. Finally, after drying the PU foams in air were

heated to 600 °C to get rid of the PU foams by burning them, and ultimately sintered at 1200 °C for 2 h in a muffle furnace. HA/PCL composite scaffold was fabricated by immersing prepared HA scaffolds in the pre-prepared PCL solution for 30 s and dried in a fume hood for 12 h at room temperature. Their study demonstrated that PCL coating increased the mechanical strength of the scaffold while subject to loading at the initial stage of in-vivo implementation. And, CaP coating for surface functionalization may enhance biological activities on the surface.

2.1.1. Solvent Casting & Particulate Leaching Methods (SCPL)

Solvent casting-particulate leaching is a technique that requires a mixer of a polymer solution with solid particles which are generally salts and having certain powder diameters. After dissolving the polymer in the solvent and adding salts into the solution in the extrusion process, solvent volatilizes and hence leaves porous structure behind. Then dried product is immersed in water to produce porous scaffold by dissolving present salts and leaching them out. The combination of this processes is called particulate leaching. Chuenjitkuntaworn et al. [11] showed that PCL/HA scaffolds based on solvent casting and particulate leaching method may be ideal scaffolds relying on morphological, physical, chemical, mechanical results and in-vivo analyzes. Adding HA within PCL improves mechanical strength by increasing density and rigidity. However, it does not have any effect on porosity. The Scanning Electron Microscopy (SEM) results showed that the number of cells on the surface increases with adding HA. That means PCL/HA scaffolds provide better cell adhesion and attachment and proliferation by modifying surface properties. Finally, histological analysis of scaffold which implanted to mouse calvarial demonstrated that PCL/HA scaffolds have higher bone tissue formation due to the high osteoconductivity thanks to the HA particles.

2.1.2. Gas Foaming & Salt Leaching Technique

Gas foaming provides to form artificial 3D porous scaffolds without use of solvents. The initial step of this technique is compression molding of polymers into the molds with high temperature. Then, solidified polymer is exposed to high pressure gas chamber for several days. Penetration of gas within the polymer generates bubbles and hence creates porosity inside the scaffold. Salt leaching is the same as aforementioned particulate leaching technique. Instead of use of one technique in a fabrication process two methods can be combined to improve performance of the scaffold. Salerno et al. [12] showed that

combination of gas foaming and particulate leaching methods for fabrication of multi-scaled PCL/HA scaffolds offers new understandings to bone tissue engineering. Composite methods described in their papers are composed of three steps which are mixing, foaming, and leaching (Figure 1). In the mixing part, PCL pellets are melted with HA nano-powders by using mixer at 70 °C, with 100 rpm for 10 min. Then, composite material is mixed with NaCl micro-particles deciding different concentration at 130 ºC, with 20 rpm for 10 min. Secondly, foaming process starts for creation and growth of gas bubbles by applying blowing agent gas at initial temperature, 70 °C and at saturation pressure, 10-18 MPa. then temperature is cooled to 35 °C and pressure is removed. The final step is leaching NaCl from the scaffold by immersing it in H_2O under stirring at RT for 2 weeks to dissolve all NaCl particles. At the end of processes 3D porous scaffold is obtained. Results of this study demonstrated that all steps in fabrication were successfully performed and desired scaffold were obtained. Also, according to cell/scaffold interaction results, adhesion, proliferation, and osteogenetic differentiation of pre-osteoblast MG63 cells within scaffold takes place in vivo. Based on all results, the study showed that combined gas foaming and salt leaching technique has potential for bone regeneration and for bone tissue engineering.

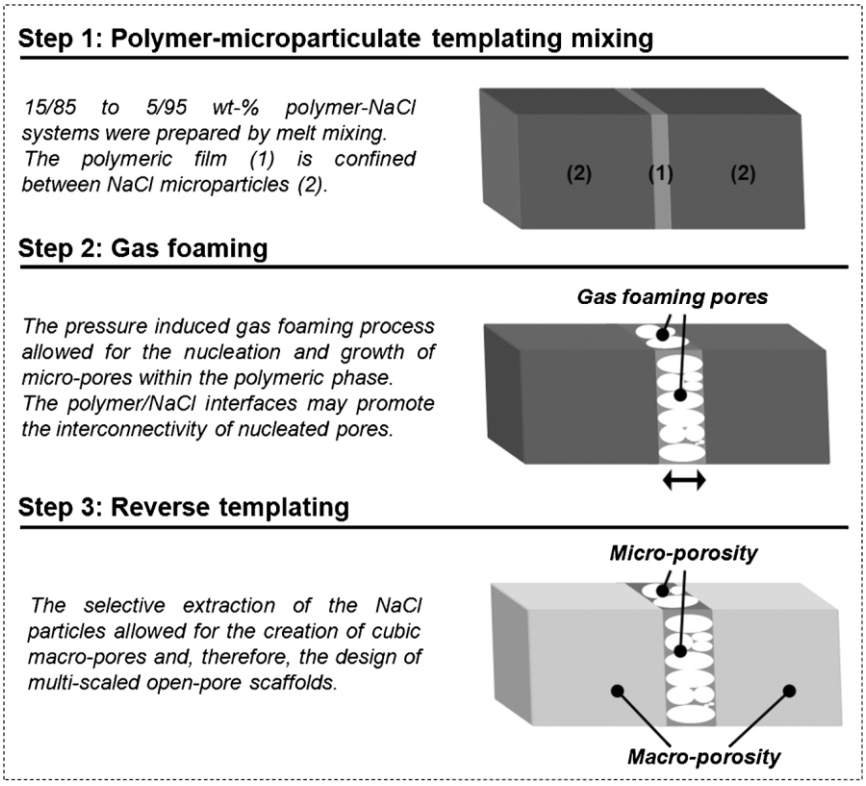

Figure 1. Gas Foaming & Salt Leaching Technique [12].

2.1.3. Electrospinning Method

Electrospinning is a technique that enables to produce polymer fiber ranging from hundreds of nanometers to several micrometers. In the process, surface tension is suppressed by electrostatic repulsion by applying adequate high voltage which is required to charge liquid droplet and to squirt fluid from the surface. The standard setup for electrospinning contains spinneret (type of syringe needle), power source for supplying high voltage to spinneret, a syringe pump and a grounded collector (Figure 2). Hassan et al. (2012) and Li et al. (2011) [16], [17] have shown that PCL/HA composite scaffold was obtained successfully by using electrospinning. In the study of Li et al., a coupling agent c-glycioxypropyltrimethoxysilane known as A-187 was used in order to improve dispersion of HA nanoparticles in PCL matrix. According to their results, HA with A187 agent had good suspension and dispersion in the solution and HA without A187 was aggregated and precipitated in PCL matrix. In addition, TEM results proved that PCL/HA fibers exhibited non-homogenous morphology with aggregated HA particles. However, PCL/A187-HA fibers had almost homogenous morphology due to the dispersive effect of the agent. Incorporation of A187-HA enhanced the tensile strength of the produced fibers significantly. However, tensile strength of fibers including HA without A187 did not show improvement. Modification of HA with A187 did not change scaffold bioactivity. However, Incorporation of HA nanoparticles into polymer enhanced scaffold bioactivity. Hassan et al. demonstrated that beadless fibers were obtained when polymer concentration was 12.5 w/v and adding HA nanoparticles increased the diameter of the produced fibers compare to pure PCL nanofibers. Result of cell viability demonstrated that osteoconductive HA nanoparticles enhanced cell growth and cell bonding ability. Both studies have shown that electrospinning is one of the preferable techniques providing nanofibers to produce porous scaffolds.

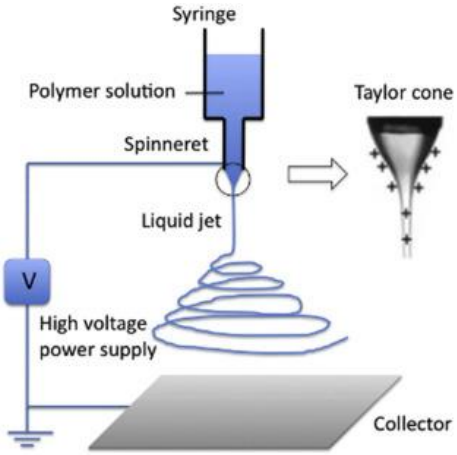

Figure 2. Representative scheme of electrospinning set-up [27].

2.1.4. Non-solvent Induced Phase Separation Technique

As in the case of solvent casting technique, Non-solvent Induced Phase Separation (NIPS) technique is actually based on removing of solvent from the solution or mixture. However, different phenomenon is that volatilization of solvent occurs in non-solvent liquid during extrusion process. In this technique there are two liquids, one of them is solvent which dissolves the polymer and other one is the non-solvent for target polymer. The important things are that solvent should be more volatile than non-solvent liquid to rapid removing of solvent from the system and they should not react with each other. After selection of proper solvent-non-solvent couple, polymer is dissolved in the solvent. Then solvent is rapidly removed from the solution by extruding in the non-solvent liquid.

NIPS technique can be also integrated with 3D printing as shown in study of Kim et al. [26] who used NIPS based 3D printing method (Figure 3) to fabricate composite micro and macro porous PCL-HA scaffold in bone tissue engineering. They used PCL and HA as a polymer and as an additive ceramic respectively. In their methods, PCL was dissolved in THF at 40 C with magnetic stirrer for 24 hours. Then, commercially bought HA nano-powders were added into the PCL/THF solution with various content (5, 10, 15, 20 %). PCL-HA/THF mixture was left to stirring at 40 C with magnetic stirrer for 24 hours. After completing 48 hours overall, mixture was cooled to the room temperature and extruded through with 640-micron nozzle diameter and deposited at 3 mm/s with 0-90 lay-down periodic pattern in ethanol bath to make the scaffold solidify. Finally, 3D scaffold was dried by getting rid of ethanol and prepared for characterizations.

Porosity and SEM analyses of this study showed that NIPS technique enables to obtain micro-macro porous scaffold because rapid volatilizing of solvent creates holes but at the same time ethanol fills those holes. After removing ethanol from scaffold, holes with ethanol become as pores filled with air and hence micro and macro porous structure is obtained. Micro-macro porosity obtained by NIPS was enhanced cell attachment and proliferation as a result of in-vitro cytocompatibility evaluation. These outputs of study suggest that the NIPS-based 3D plotting method is very useful in the production of porous PCL-based composite scaffolds with the controlled macro/micro-porous structure high mechanical features, and good bioactivity. In addition, the present method can be applied to a variety of biocompatible, biodegradable polymers, even with bioactive inorganic phases, thus finding very useful applications in bone tissue regeneration.

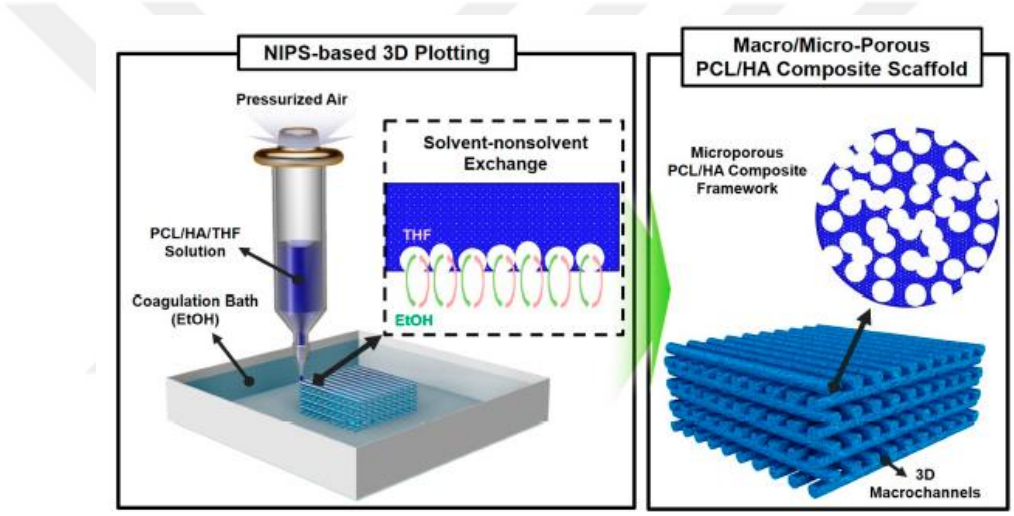

Figure 3. Illustration of NIPS based 3D printing of PCL-HA solution to produce controlled macro porous structure [26].

2.1.5. Wired Network Modelling Method

Some fabrication techniques may not guarantee the best and perfect structure due to the scaffold collapsing during manufacturing processes. In order to prevent possibility of collapsing, the wired-network molding has been developed and applied in several studies to fabricate scaffold in bone tissue engineering.

Fabrication of 3D hydrogel scaffold by using wired-network molding, at the first time, has been proposed by study of Lee et al. [13] and provides the interconnectivity, effective mass production, and low cost. When it comes to fabrication process, steps are the following. First thing is to make cubic base cage (Figure 4-L(A)), then metal wires having

rectangular cross section are inserted as vertical sidewall columns which have certain gap in between (Figure 4-L(B), 4-L(C), 4-L(D)). Then the first set of same metal wires are placed on the bottom of base cage (Figure 4-R(A)) then other sets are inserted on top of each other with 0-90º periodic lay-dawn pattern (Figure 4-R(B), 4-4-R(C), 4-R(D)). Final mold has well precise interconnected wired-network (Figure 4-R(D)).

The wired network molding also was used by Cho et al. [14] to fabricate well-interconnected polycaprolactone/hydroxyapatite composite scaffolds in bone tissue engineering. Furthermore, The WNM and NIPS methods was combined by Sohn et al. [15] for fabrication of dual-pore scaffolds. Both studies have demonstrated that well controlled interconnected porous scaffold was obtained by using WNM technique and hence cell attachment and proliferation were increased due to the addition of HA powders and well interconnectivity.

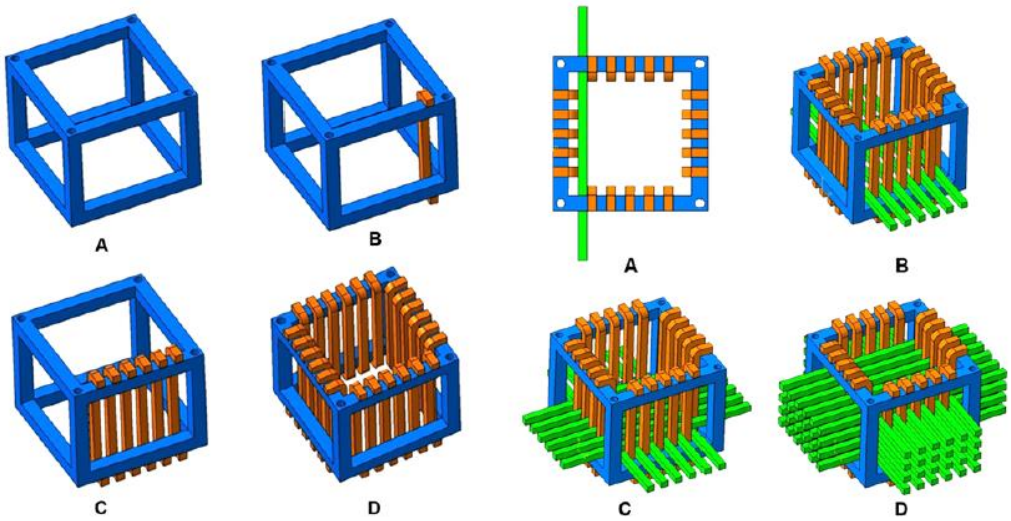

Figure 4. Scheme of Wired-Network Molding; (L:Left, R:Right) [13].

2.1.6. Solid Free Form Method

Computer aided design and computer-based control systems led to manufacturing of well-designed and well-controlled structures in high precision for many research fields. Solid free form technique is comprehensive and roof term including FDM, SLA, SLS, 3D printing in itself. Among different method types of SFF, Fused Deposition Method (FDM) is very popular because it provides easy way to deposit material to form 3D structure in high precision.

The basic principle of FDM is the following. Thermoplastic materials are fed to the system as filament and melted by heat nozzle and deposited layer by layer on bed in cartesian coordinates. Shor et al. [19] developed new fabrication system called as precision extrusion deposition (PED) which is made up of mini extruder mounted on high precision positioning system (Figure 5). The advantages of this system are that materials in pellet or granulated form can be used which offers avoiding of filament making process and increases variety of material used in the system.

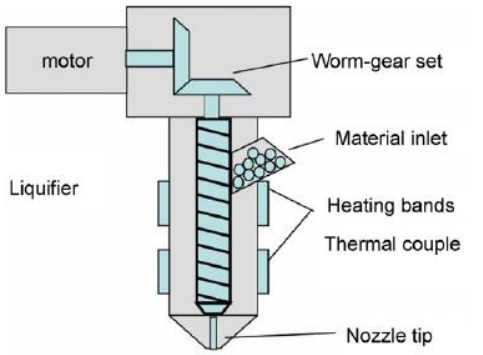

Figure 5. Representative image of PED in SFF including all parts [19].

The materials which can be pure PCL or mixture of PCL pellets and HA powders are fed from material inlet part. Delivered materials are melted by two heating bands in the liquefier part then molten material is extruded due to the pressure created by turning screw to the outside and finally by using nozzle tip fused material is deposited. Their study and results demonstrated the viability of the PED process to the fabricate PCL and PCL–HA composite scaffolds having necessary mechanical property, structural integrity, controlled pore size and pore interconnectivity desired for bone tissue engineering.

Another novel fabrication method of SFF developed by Kim et al. [20] is that multi-head deposition system (MHDS) which is one of the SFF method to fabricate polycaprolactone/hydroxyapatite (PCL/HA) scaffolds. The MHDS has a motion controller for the x-y-z-axis motion system and four isolated deposition heads, including a pneumatic controller and a temperature controller (Figure 6). Two deposition heads were placed at the front of the x–y axis, while the other two heads were assembled at the back of the system.

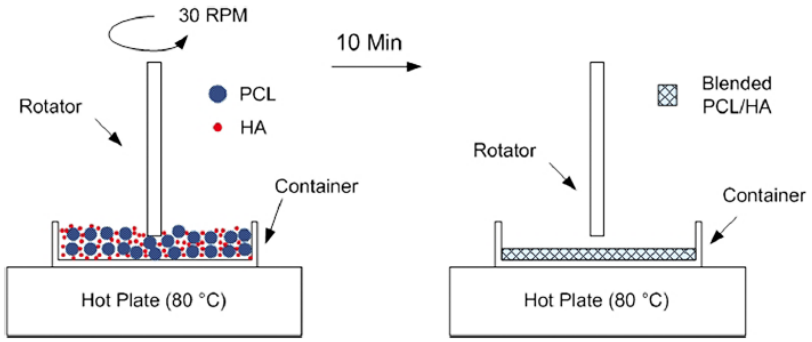

Figure 6. Schematic of Multi-Head Deposition System [20].

Park et al. [21] used a bio-plotting system made up of computer control system to control pressure nozzle size and plotting velocity on the x-y-z stage, heating jacket, nozzle, pressure pump (Figure 7). PCL-HA is melted in the heat jacket of the system and each layer is deposited on top of each other with 0-90 lay down pattern on the stage and printing parameters are controlled by computer system. In this study, they fabricated PCL, PCL/HA, and PCL/HA/ SP scaffolds using a 3D plotting system. All three scaffolds exhibited well-defined architecture and uniform pore structure.

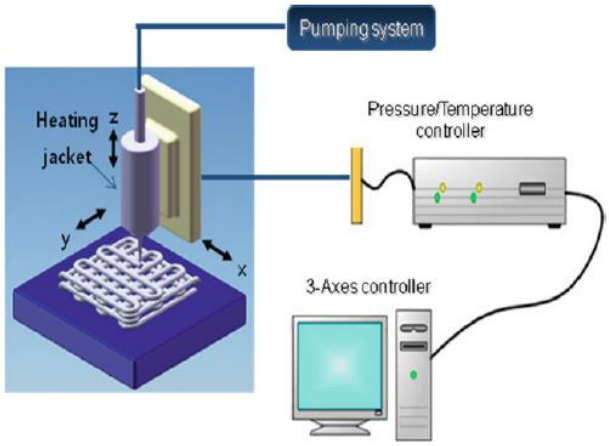

Figure 7. Schematic of 3D Plotting [21]

As a result of fabrication methods in the literature, polymer impregnation methods can be used primarily for coating, which is not suited for producing composite scaffolds with micro-scale pores. Salt leaching is used in combination with standard scaffold fabrication techniques as an add-on post-process resulting in a more tedious and lengthy process. Gas foaming requires high temperature to melt polymer into mold and high pressure for solidification. It requires mold design and production as well. Wired network modeling

prevents materials from collapsing. However, it requires molding design and fabrication. It is not flexible hence increases fabrication cost. Fused deposition modeling (FDM) based 3D printing allows to build controlled scaffolds architectures in the x-y-z space. Nevertheless, it is not usually capable of incorporating micropores within scaffold due to the inherent melting process and the positioning and deposition resolution limit. Electrospinning is more suitable for making fiber based even in nanoscale materials but not quite suited to produce composite substrates with well-controlled macro-porosity and pore size. Most of these techniques are time consuming and post processing, require specialized equipment or are based on solvents. As discussed in more detail in the literature review chapter, these techniques suffer from cost and time ineffectiveness, are not readily suitable for integration to 3D printing and do not allow for the formation of well distributed pores and reproduction of porous scaffolds.

Among these fabrication techniques, a more recent technique known as non-solvent induced phase separation (NIPS) is known to be advantageous in terms of obtaining desired multi scale porosity mostly used for the production of membranes [23], [24], [25].

Kim et. [26] used NIPS technique and has demonstrated to have the potential to induce micro-pores in substrates/scaffolds that potentially can be printed or produced with controlled macro-pores in fairly wide range of pore scale (micro-meso and macro scale) due to the controllability of phase separation and phase exchange processes. Towards that goal, integration of NIPS technique with 3D printing was studied by Kim et al. to fabricate a 3D PCL-HA scaffold [26]. However, they did not examine the effects of thickness and PCL concentration on PCL-HA scaffolds.

2.2. Surface coating with iCVD

In the literature, p(HEMA-*co*-EDGMA) microbeads were synthesized by suspension polymerization technique by Ayhan et al. [28]. Their study showed that 3T3 and MDBK cell lines significantly attached on these microbeads. Bose et al. fabricated p(HEMA) thin film via ICVD and they showed that thin films were nontoxic and have good adhesive property for fibroblast cells [29]. p(HEMA) was produced by thermally initiated free radical polymerization by Passos et al. They also demonstrated biocompatibility of p(HEMA) without showing apoptosis [30]. Giglio et al. used electro-polymerization technique to produce p(HEMA) based thin films. Their study showed that coated surface with p(HEMA) has significant contribution on cell attachment [31]. Ma et al showed that

PCL electrospun substrate can be coated with ICVD [32]. Cheng et al [33] studied that 3D printed scaffolds coated with p(HEMA-*co*-EGDMA) via ICVD and they achieved hydrophilic surface. Contact angle measurement of the study of Gupta et al [34] demonstrated that surface properties of pores was tuned by iCVD nanocoating. In this study, for the first time, we will show that surface coating of PCL/nHA composite thick films using iCVD.

Chapter 3

Background

3.1. Biology of Bone

Bone tissue is one of the key essential tissue types in backboned organisms and is composed of the skeleton system, which protects and supports various organs and enables the body to move from one location to another. Bone produces red and white blood cells which play important roles in blood circulatory system and immune system respectively, and stores minerals. Bones have complex structures both internally and externally and they vary in terms of shape, size and geometry. Due to their structural differences, bones can be classified into long, short, flat, irregular, and sesamoid bones. Typical long bones such as femur or humerus contain two distinct parts called cortical (compact) and trabecular (spongy or cancellous) bones.

The former, cortical bone forms the hard-outer protective layers surrounding the internal cavity of the bone. Cortical bone constitutes 80% of skeletal mass in the human body and is the load bearing component due to its high rigidity and high resistivity against torsion and bending. It has less porosity and hence less surface area than trabecular bone.

The latter, trabecular bone, is found at both ends of long bones and is responsible for 20% of the total skeleton mass. It has an open honeycomb morphology and has lower elastic modulus than cortical bone due to its high porosity. It has higher ratio of surface area to volume that makes it weaker and flexible, on the other hand, this higher surface area provides a suitable medium for metabolic activities such as ion exchange. In addition, trabecular bone contains red bone marrow forming blood cells such as red and white blood cells and platelets (thrombocytes).

In terms of its material composition, bone can be considered as a natural composite material including organic and inorganic molecules at the same time. It consists mainly

of collagen fibers and bone minerals as organic and inorganic constituents, respectively. In vivo bone (bone inside the living body) also contains 10% - 20% water. While bone minerals constitute about 60 - 70 % of bone-dry mass, rest of it mostly contains collagen and a small amount of molecules such as inorganic salts and proteins. Mineral composition of bone can be thought as Hydroxyapatite (HA) which is mainly based on calcium and phosphate elements with the chemical formula $Ca_{10}(PO_4)_6(OH)_2$. The ratio of calcium to phosphate in HA chemical formula is 1.67. However, in vivo bone has range from 1.37 to 1.87 because of the complexity of bone mineral containing different additional ionic substances such as zinc, silicon, and carbonate.

Bone does not have an unifactorial structure, i.e.it is composed of different components and morphology. Therefore, its young modulus and strength vary within itself. Table 1 shows Young's moduli, tensile and compressive strengths of long bone (femur) with respect to material type and direction, respectively (Table 1 and 2).

Table 1. Modulus of elasticity of materials of typical long bone (femur) [35]

Material	**Young's Modulus (MPa)**
Bone mineral (HA)	80,000
Collagen	6,000
Longitudinal Cortical Bone	11,000-21,000
Transverse Cortical Bone	5,000-13,000

Table 2. Compressive and tensile strength of typical long bone (femur) [35]

Strength (MPa)	**Direction, Longitudinal**	**Direction, Transversal**
Compressive	60-70	~50
Tensile	70-280	~50

3.2. Bone fracture healing

There are four main phases in bone fracture healing. First, healing starts with hematoma phase also called the inflammatory phase where the volume of tissue increases during inflammation. In this phase, fracture site is filled by hematoma which provides temporary scaffold and suitable medium for differentiation of stem cells into cartilage, bone and fibrous tissue types. At this phase, both biological factors generally known as growth factors are released and applied mechanical loads and stimuli such as strain or hydrostatic pressure play integral part in the bone healing by regulating activities of mesenchymal

stem cells (MSC), [36], [37], [38]. MSCs are multipotent cells having ability to differentiate to various cell types and are the main providers for bone formation [39].

The healing continues with soft callus phase. Activities of endothelial and skeletal cells form cartilaginous callus (soft callus) which fills gaps between bone fragments by connecting them. Soft callus then transforms to hard callus. There are two mechanisms in bone formation which are intramembranous and endochondral ossifications. In the first one, bone tissue is formed directly by differentiation of MSCs to osteoblast cells via anabolic process. In the second, extracellular matrix which is a 3D biological structure providing structural and biochemical support and networking extracellular molecules such as enzymes, glycoproteins, and collagen is formed by differentiation of MSCs to chondrocytes which produce the cartilage tissue. ECM is mineralized until apoptosis and then osteoblast cells attack this dead structure (calcified ECM) and form bone tissue.

Other mechanisms are primary and secondary bone healing. In the primary bone healing, callus formation does not exist. Bone healing between bony fragments which are connected and fixed very well under implantation compression occurs via only osteoblasts and osteoclasts activities [37], [40]. In the secondary bone healing, which is the most widespread healing type in the bone formation processes appears if small amount of motion exists between fragments. This motion is responsible of soft callus formation and leads to intramembranous and endochondral ossifications during secondary bone healing [37], [41]. Secondary healing is initiated by anabolic phase. However, catabolic and anabolic activities occur at the same time when soft callus volume is diminished. Coordination of osteoblast and osteoclast activities over several months leads to beginning of remodeling phase in which callus tissues are broken down and lamellar bone is formed [42], [43].

3.3. Theory, Mechanism and Effecting Parameters of NIPS

Non-solvent induced phase separation (NIPS) process is controlled mainly by two thermodynamic mechanisms which are instantaneous and delayed demixing processes. Thermodynamic aspects of those processes are discussed by Strathmann et al. [44] by using ternary phase diagram which can be utilized for analyzing the thermodynamics of precipitation processes of membranes. This phase diagram is represented as a triangle and each of its corner represents one component as either polymer, solvent or non-solvent as

shown in Figure 8. However, any arbitrary point inside the triangle indicates a mixture of all three components.

There are two regions in the system: in the one-phase region, all components have miscibility with each other, and the two-phase region contains polymer-poor and polymer-rich phases which will be separated from each other and form pores and the membrane matrix, respectively [45]. The line connecting any of the two thermodynamically at equilibrium mixtures from each other is called tie line. Binodal curve term is used for liquid-liquid phase boundary. Demixing of a composition into two liquid phases requires to pass the binodal curve. In other words, passing the binodal curve guarantees demixing of every composition into two liquid phases having different composition but are thermodynamically at equilibrium [24]. Instantaneous demixing is a rapid separation of the liquid phase into two different liquid compositions. As can be seen in the ternary diagram (Figure 8), the composition profile rapidly reaches and cuts the binodal curve, and the composition path is shorter. In this process, polymer precipitates quickly and hence solid film rapidly forms after soaking the cast into coagulation bath. Instantaneous demixing provides highly porous sub-morphology especially with finger-like macrovoids and porous thin skin layers. On the other hand, in the case of delayed mixing process which exceeds the binodal curve as seen figure b, all mechanisms observed in the first case slow down resulting in spongy-like porous sublayers, and a relatively denser top layer. Formation of macrovoids which may show finger-like or spongy-like morphology may be observed as a result of different mechanisms as suggested by several researchers as discussed next.

According to Matz [46] and Frommer and Lancet [47], surface tension gradient drives interfacial hydrodynamic instability that starts macrovoid formation. Strathmann et al. [48] suggested that macrovoid morphology is determined by precipitation rate. The reason of macrovoid formation, according to Ray et al., is that steep concentration gradient near the surface induces excess intermolecular potential gradients. Smolders et al. [49] and Boom et al. [50] proposed that solvent diffusion withdrawing from polymer solution is resulting in macrovoids.

The mechanism of demixing depends on the miscibility between solvent and non-solvent. The higher mutual miscibility, the faster demixing i.e. instantaneous demixing occurs. In other words, rate of demixing increases with increase of the miscibility between solvent and coagulation bath [51].

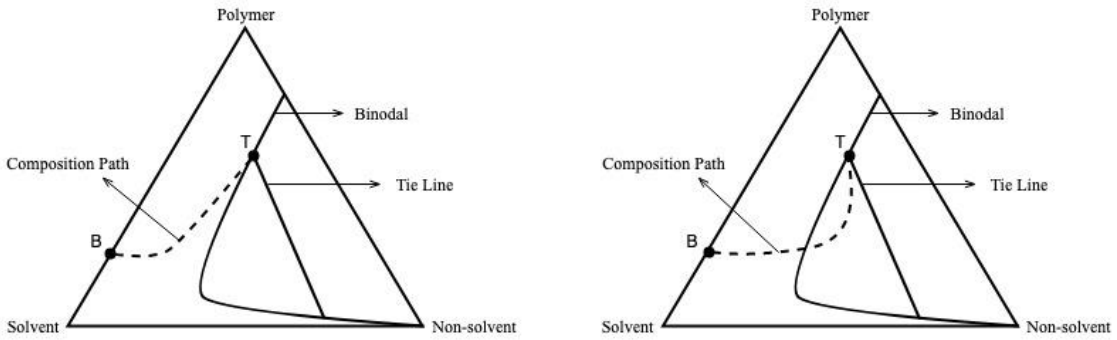

Figure 8. Ternary diagram for instantaneous (left) and delayed demixing (right).

Effect of polymer solution concentration on porosity and morphology in NIPS

Every polymer has its own chemical structure and molar mass property, those directly affect the membrane performance, morphology and property in terms of hydrophilicity, adsorption, chemical and thermal stability. In the NIPS process, limitations based on solvent and non-solvents performance in the phase exchange process is directly linked to the choice of the polymer. Also, not only the choice of polymer but also the polymer solution concentration is one of the key parameters in membrane formation and membrane morphology. Solution concentration directly affects the type of macrovoid morphology. According to study of Jung et al. [23], finger-like macrovoids were observed more by using lower concentration polymer solution. However, spongy-like/spherulitic morphology (TIPS) was observed at the lower part of the surface specifically for the higher polymer concentration solutions. As the concentration of polymer solution increases, the porosity morphology changes from finger-like (NIPS) to spherulitic structure (TIPS) and porosity decreases.

Effect of concentration of coagulation bath on porosity and morphology

Like polymers, solvents also have different properties and key features which are effective in the outcome of the NIPS process. First, while chosen polymer must be dissolved by chosen solvent, it should not be dissolvable by the used non-solvent. Furthermore, mutual affinity or miscibility between solvent and non-solvent should be higher.

Increased concentration of the solvent in the coagulation bath decreases the concentration gradient and diffusion rate of the solvent from dope to the nonsolvent and therefore its effect during NIPS becomes less visible. NIPS morphology (macrovoids, finger-like) is suppressed by TIPS morphology (spherulites) with increase of solvent concentration in

coagulation bath because of decrease of concentration gradient and reduction of mass exchange rate between solvent and nonsolvent. Lower exchange rate delays demixing (liquid-liquid phase separation) and hence morphology ends up with denser surface. As a result, NIPS effect is more dominant at low solvent concentration in coagulation bath. The other parameter is the crystallinity phenomena in the NIPS-TIPS system. Crystallinity increases as the fraction of solvent in coagulation bath increases from 0 to 60 % at constant low temperature such as 5. However, after 60% of solvent content, the effect on the NIPS process disappears. Therefore, there will be no phase exchange after certain maximum amount of solvent fraction [23].

Effect of coagulation bath temperature on porosity and morphology

The other parameter affecting on membrane morphology is the coagulation bath temperature. Nevertheless, more solvent is necessary in NIPS method that makes the process infeasible for large scale applications. However, study of Jung et al. demonstrated that as the temperature of coagulation bath increases, the porosity of structure decreases turning the morphology of porosity from finger-like (macrovoids) to spongy-like (spherulitic) morphology [23].

Effect of additives on porosity and morphology

Addition of inorganic powders/particles increases the hydrophilicity of the solution and hence increases the porosity since shrinkage of solution decreases as the concentration of additives increases. As the shrinkage increases, expansion of the deposition in the nonsolvent phase increases and hence this creates higher voids in the structure. Incorporation of additives induces instantaneous demixing by closing the polymer solution concentration to binodal curve. In addition, additives contribute substantial affinity towards non-solvent that creates porous surface.

Effect of membrane thickness on porosity and morphology

Several studies have showed that there is a critical thickness where the transition from spongy-like to finger like structure occurs during membrane formation. Under a certain critical thickness, macrovoids within membrane exhibit spongy-like morphology. However, if the membrane thickness exceeds the critical thickness, macrovoids morphology turns from spongy-like to finger-like structure. Also, finger-like formation gradually increases with increase of membrane thickness. There are several reasons behind those different morphologies. The exchange rate of solvent and non-solvent is not

affected by membrane thickness if the thickness is greater than critical thickness. Because membrane thickness and concentration profile of solvent and non-solvent do not influence each other with the assumption of infinite boundary condition of membrane thickness (L = infinity). On the other hand, if the membrane thickness is lower than critical thickness, the spongy-like morphology forms since the exchange rate of solvent to non-solvent is strongly influenced by boundary condition. Due to small amount of solvent coming with lower thickness, non-solvent concentration will be higher than the thicker membranes (considered as infinite) and therefore result in dominant exchange process between solvent and non-solvent.

Vogrin et al. [52] demonstrated that macrovoids were formed when the membrane thickness is 500 microns, but they were not seen when membrane thickness is 150 microns and 300 microns. This result may be interpreted as while the membranes having below the critical thickness display a spongy-like structure, the membranes with thicknesses above the critical value display a finger-like structure.

Li and Chung [53] reported that a spongy-like structure was observed when the membrane thickness reached a value of 0.76 microns. With an increasing membrane thickness the appearance of macrovoids and finger-like structure was observed fully above a thickness of 2 microns.

Result of Conesa et al. [54] showed that macrovoid dimensions in length and width increases with increase of membrane thickness. In addition, macrovoids were not present in membranes with a 35-40-micron thickness.

According to the study of Ren et al. [55], spongy-like morphology disappeared, and finger-like structure appeared when the membrane thickness increased from 15 microns to 24 microns. In addition, fully developed finger-like morphology occurred at a thickness value of 40 micron. These observations suggested that membrane morphology is highly dominated by the variation of membrane thicknesses.

The cross-section morphology of thickness-gradient membranes in the study of Ren et al. [56] demonstrated that when the membrane thickness in between 0 and 12 microns spongy-like structure appeared. However, several finger-like macrovoids were observed in membranes with thickness of 16 microns. In addition, when the membrane thickness was 68 microns, finger-like structure fully covered the membrane morphology.

Ren et al. [57] showed that membrane morphology changes from spongy-like structure to finger-like structure with the increase of membrane thickness from below critical thickness to above critical thickness for the flat sheet membranes composed of PEI/NMP/NS.

3.4. Theory of Micro Computed Tomography

Micro computed tomography (micro-CT) is a device that forms high resolution 3D images by using X-rays. It is similar to a hospital CT scan but on a smaller scale with an augmented resolution. Among the imaging techniques, micro-CT imaging neither destructs the original object nor damages biological specimens in most cases. Sample preparation, staining, and slicing are not required. Only single scanning can visualize the structure of the object and construct 3D image at a high resolution. These advantages together with its simple use turns the micro-CT imaging into a desired technique for sample characterization. More specifically, micro-CT device enables the characterization of the internal micro-structure of a 3D object in terms of structure morphology, geometry, porosity and pore size distribution. It does provide these features through micro-CT scans providing a 3D image of an object by reconstructing 2D sliced raw images.

In order to understand the role of micro-CT in design and characterization processes, which is one of the key characterization tools used in this thesis, its basic working principles need to be understood and therefore are reviewed shortly in this section. This process can be summarized in four basic steps:

i. Generation of X-rays
ii. Absorption/Transmission of X-rays.
iii. Sample rotation to form a 3D image.
iv. Reconstruction of projection images into virtual slices

i. Generating X-rays

Electromagnetic radiation in the form of X-rays, is generated by electric currents and hence electrons produced in a cathode where tungsten and copper are used as a target. X-rays are emitted by a target and transmitted to an object. A micro-focus x-ray source has two types of projections. In the simplest case, source can be considered as a parallel x-ray beam (Figure 9). In this approach, each partial parallel beam coming from a source is absorbed inside the 3D sample and transmitted to detector. Inside the object, each point

interacts with the beam and contains absorption information. Integration of absorption information inside the sample contributes to the formation of each point on the shadow image.

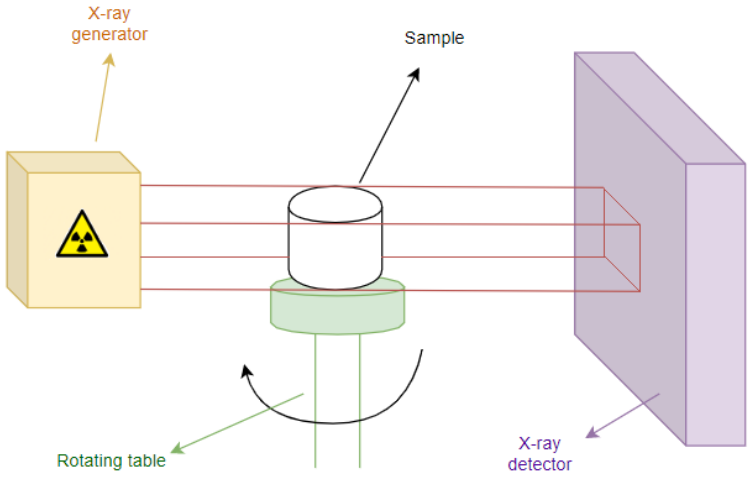

Figure 9. Scanning principle of CT using parallel X-ray beam source.

However, most of X-ray sources cannot generate parallel X-ray beams instead they produce cone beams emerging from a spot (Figure 10). Due to the nonhomogeneous thickness distribution inside the object, the reconstructed slices have some distortions far from the optical axis. In other words, transmitted rays cannot be projected onto the same row of the detector due property differences of the front and back of the object.

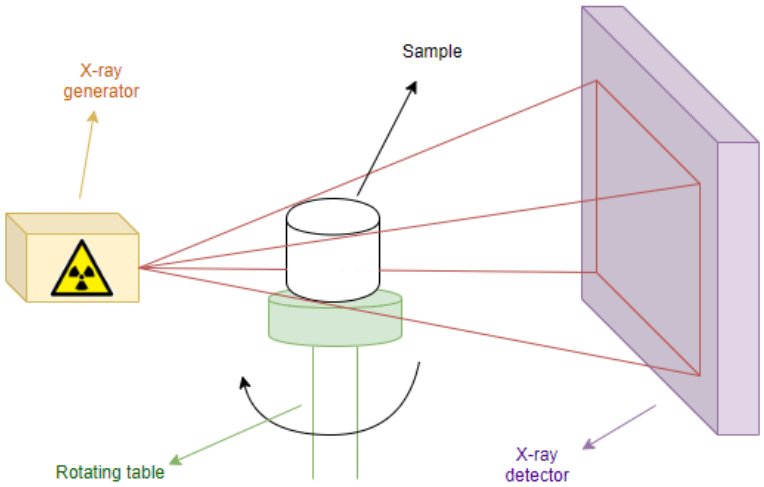

Figure 10. Scanning principle of CT using cone beam source.

ii. Absorption of X-rays

There are two important optical responses that occur in the imaging processes within a micro-CT which are absorption and transmission through the object. While some x-ray beams are absorbed partially or totally by object depending on material type, others are transmitted to the detector. Absorption of x-rays can be expressed by the x-ray attenuation of the material.

The X-ray attenuation is expressed as:

$$I_1 = I_0 . e^{-\mu t}$$

where:

I_0 = inlet X-ray intensity.

I_1 = outlet X-ray intensity.

μ = the X-ray attenuation coefficient.

t = the thickness of the absorbing material.

Detector records unabsorbed X-rays emerging from the object and so a single radiographic image is produced, similar to an X-ray taken for a broken bone a patient would have taken in a hospital. Amount of absorption is mainly affected by material type. Denser materials, such as bone, absorb X-rays more than less dense materials. In other words, for less dense materials such as tissues and polymers, X-ray transmission is higher than for dense materials. Here, term of "dense material" means thicker materials with higher atomic number. For instance, lead element blocks the X-rays well due to the its high atomic number therefore it is preferred as a shielding material around the X-ray devices. On the other hand, it is difficult to get an image working with low atomic number elements such as Beryllium because of its low atomic number and hence low attenuation rate. Attenuation rate increases as the atomic number increases. Therefore, it can be easily seen as expressed in Equation1 that at high attenuation rate (for dense material), intensity (arrived x-ray information to detector) will be low.

iii. Sample rotation to form 3D image

After starting the acquisition, sample is rotated by rotating sample holder with small rotation angles generally less than 0.5-0.7 degree (default value). Until the completion of 360 degrees, at each step a new projection image is taken. Low degree ratio (rotation step) which means finer step sizes (small value), is favorable for large objects due to their contrast. By doing so, higher number of image files and hence finer reconstructed images are obtained at longer scanning times and higher computer's storage and memory requirement. Increasing the rotation step, i.e. a coarser step size (large value), is an effective solution for reducing the scanning time and computer's memory and storage if the sample is a small object and has symmetry.

iv. Reconstruction of Projection Images into Virtual Slices

Reconstruction can be simply explained as the computing process of the projection images containing internal structural information of the object. At the end of the process, a series of reconstruction images, i.e. cross-sectional images or slices, are obtained. This process relies on Feldkamp, Davis, and Kemp (FDK) cone beam reconstruction algorithm which is a form of filtered back projection (FBP). FBP is an analytic reconstruction algorithm designed to handle the limitations of conventional back-projection by applying a convolution filter to remove blurring. Until recently, it was the main method for reconstruction of the cross-sectional images [58], [59], [60].

Chapter 4

Experimental Procedure and Characterization

In this chapter, the main steps of the experimental procedure of the solution preparation using the NIPS process is presented first which is used both for the film and 3D scaffolds as summarized next. Then, the iCVD process is shortly introduced which is used for surface functionalization. Finally, all relevant characterization techniques including bone mineral density calculation, morphological analysis with micro-CT and porosity evaluation with gas pycnometer, scanning electron microscopy with eds analysis, mechanical properties evaluation, contact angle measurement, viscosity analysis with rheometer, for surface functionalization contact angle measurement, FTIR and ellipsometer characterizations are performed and discussed.

4.1. Solution Preparation

PCL pellets (Mn 80,000) and nHA powder (< 200 nm) were purchased from Sigma Aldrich (St. Louis, MO, USA). The experiment was conducted with 10% and 12.5% PCL/THF (w/v) solution at 40 °C. First, PCL pellets were added gradually into THF solvent. After 24 hours of magnetic stirring, PCL was completely dissolved, and the solution turned into a transparent color. Then, nHA was put into the solution (0%, 10%, 20% w/w). Again, the solution was stirred for 24 hours to get a homogenous slurry. Representative scheme of the NIPS solution and its use for scaffold preparation follow that shown in Figure 11.

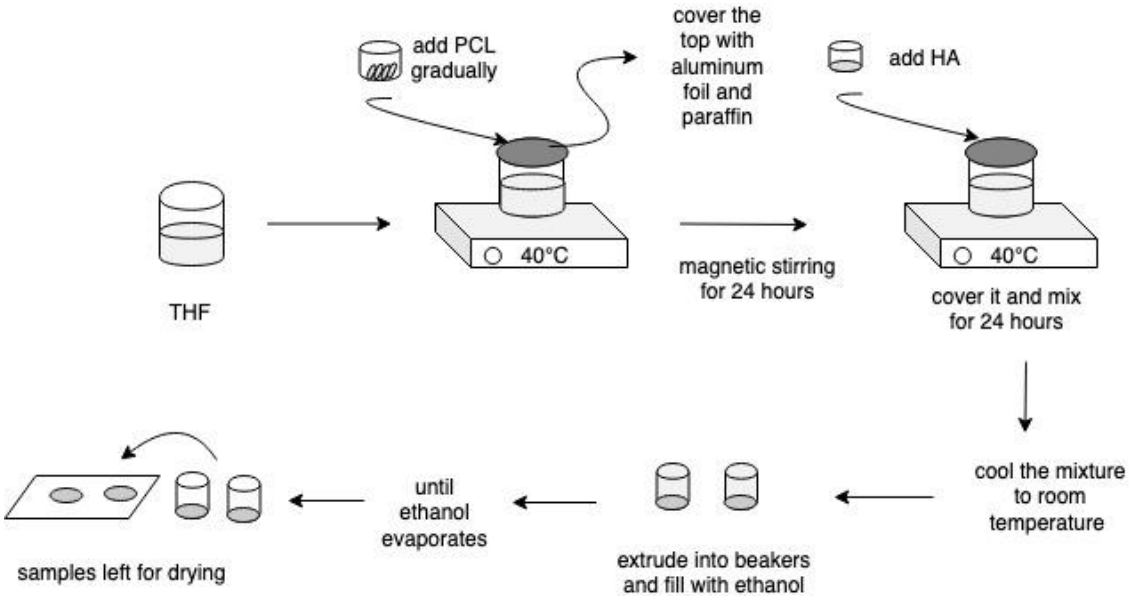

Figure 11. Schematic representation of experimental procedure of NIPS.

4.2. Scaffold Preparation

4.2.1. Fabrication of Film Scaffolds

When the temperature of the NIPS solution cooled down to room temperature, as discussed in the previous section, with the help of a glass measuring pipette, the mixture was added into beakers, which were then entirely filled with ethanol. Solidification of these samples were achieved through ethanol evaporation. Finally, the round-shaped samples, in this thesis referred to as film scaffolds, were taken out of the beakers and were left to dry in air.

4.2.2. Fabrication Trial of 3D Scaffolds

To test the printability of the material produced via NIPS, 12.5% PCL with 10% nHA solution was used for fabrication of 3D scaffolds with Celllink BioX Bioprinter (Boston, Massachusetts, United States). Due to low viscosity of 10 % PCL solution with 10% nHA, 12.5 % PCL with that of nHA slurry was selected. In order to obtain well controlled scaffolds with uniform strut width size and thickness, print parameters had to be optimized. After several trials, based on the use of a 0.58 mm diameter nozzle, the pneumatic pressure and print speed were optimized as 47 kPa and 10 mm/s, respectively in order to meet optimal solidification of deposited layers in ethanol while ensuring satisfactory attachment of newly deposited layers to previous deposited layers. Desired

strut diameter of CAD model was 0.5 mm. The distance between adjacent struts was 2.5 mm in order to prevent collision of deposited struts which are known to expand during printing. It is noted that this test was performed in this thesis to demonstrate the printability of NIPS produced samples and detailed analysis and effect on the performance and geometry of produced scaffolds are within the scope of future studies. The main challenges of integration NIPS with 3D printing is to obtain 3D scaffold without collapsing. To overcome this challenge, print speed and extrusion feed rate in terms of pressure (kPa) should be optimized. Because, solidification of deposited struts takes certain time in ethanol bath. Failure of solidification is the main reason of collapsing. Each next layer should be deposited well on top of each solid previously deposited struts. Final result will give well build 3D scaffold under optimized circumstances.

4.3. Surface Functionalization of Film Scaffolds via iCVD

Initiated chemical vapor deposition (iCVD) is one of the most powerful technique used in polymer depositions and it was utilized in this thesis to obtain functionalized surface of film scaffolds. Among other CVD techniques, iCVD enables to coat responsive and functional polymers as well as hydrogels by free radical polymerization. It has no disadvantageous solvent effect since the monomer is fed in the vapor phase into the reactor. During the deposition, initiator is introduced to the heated filaments for decomposition and radical formation. Monomers and crosslinkers are fed in the gas phase. All of the monomer, crosslinking agent and the initiator then start the polymerization onto the substrate which is cooler than the filaments. A schematic of the iCVD technique is given in Figure 12. Conformal deposition is the key factor for the scaffold surface functionalization. Homogeneous distribution and unchanged surface topography make iCVD very suitable for our targeted application of the produced samples [61].

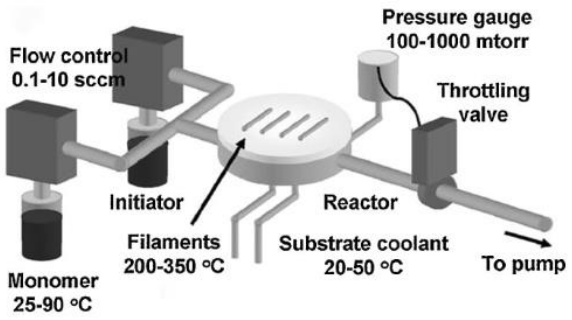

Figure 12. Schematic presentation of the iCVD process with monomer and initiator inlets, outlet, filaments and other parts [62]

The top and bottom surface of the produced film scaffolds using NIPS were coated with poly(2-hydroxyethyl methacrylate-*co*-ethylene glycol dimethacrylate) (p(HEMA-*co*-EGDMA)) using this iCVD process. The monomer HEMA and the crosslinker EGDMA were heated in the metal jars to 75°C and 95°C, respectively. The initiator tert-butyl peroxide (TBPO) was kept at room temperature. Substrate temperature was adjusted to 25°C while filament temperature was 200°C. Reaction pressure was tuned at 100 mTorr throughout the polymerization. The flow rates of HEMA, EGDMA, TBPO and nitrogen were 1.7 sccm, 0.243 sccm, 0.94 sccm, 1.1 sccm, respectively. A laser interferometry was used during the deposition to monitor the thickness of the samples. Deposition was ended when the film thickness of 250 nm was observed.

4.4. Characterization

4.4.1. Bone Mineral Density Calculation

Bruker Micro-CT 1172 device was calibrated with 0.25 and 0.75 g/cm^3 HA phantoms. After the calibration, based on Otsu's thresholding method, Hounsfield unit and bone mineral density of 10% PCL scaffolds having various nHA content (0, 10, 20 %) was calculated by CTan software (version 1.18) for constructed VOIs. Histogram results of HU and BMD were saved and plotted. Theoretical BMD values were calculated by using following formulae.

$$w_{x_{HA}} = \frac{\text{amount of HA in specimen}}{\text{amount of HA} + \text{amount of PCL in specimen}}$$

$BMD_{exp} = w_{x_{HA}} * \rho_{HA}$where $w_{x_{HA}}$ is weight fraction of nHA, BMD_{exp} is the bone mineral density of scaffolds based on fraction density of nHA in the scaffolds.

4.4.2. Morphological Analysis with micro-CT

Structure morphology within scaffolds in terms of overall porosity, pore size distribution, pore shape and pore network anisotropy were evaluated by micro-CT (SkyScan 1172; Bruker-microCT, Kontich, Belgium). Scanning mode settings are listed in Table 3 for film scaffolds and in Table 5 for 3D scaffolds. After scanning was finished, 2D slices are reconstructed by NRecon software to obtain 3D structure of the object. Settings for reconstruction process are also listed in Table 5. Morphology images of specimens were obtained by DataViewer software for several different slices of cross section. In the CTan

software, 101 slices were selected for calculation of roughly uniform and centrally located region of the scaffold instead of the entire scaffold to reduce usage of computer's memory. Round shaped ROI was applied through these selected 101 slices to create a comparable Volume of interest (VOI). Lower and upper threshold values were set to auto and 255 in gray scale, respectively, in order to match original CT image to a binary image. To examine anisotropy of pores within scaffolds, first, otsu threshold method was applied to previously selected VOIs in custom processing page and then inverse of image with ROI was taken. 3D analysis including anisotropy calculation was conducted to extract all relevant parameters of the pore network. In addition, 3D model tool was applied to obtain the microstructure of the scaffold pore network.

Table 3. Scanning parameters of SkyScan 1172 Micro-CT device for film scaffolds

Camera Pixel Size (µm)	Resolution Pixels	Image Pixel Size (µm)	Source Voltage (kV)	Exposure Time (ms)	Rotation Step (degree)	Filter
8.75	1336x2000	12.95	90	370	0.4	None

Table 4. Scanning parameters of SkyScan 1172 Micro-CT device for 3D scaffold

Camera Pixel Size (µm)	Resolution Pixels	Image Pixel Size (µm)	Source Voltage (kV)	Exposure Time (ms)	Rotation Step (degree)	Filter
8.75	2672x4000	0.97	40	1490	0.25	None

Table 5. Reconstruction parameters of NRecon software.

Ring Artifact Correction	Beam Hardening Reduction (%)	Results Image Pixels
6	20	2000x 2000

4.4.3. Porosity Evaluation with Gas Pycnometer

In order to calculate the porosity based on the measured density of the fabricated scaffolds, micromeritics gas (helium) first pycnometer was used to find density of commercially bought PCL and nHA by measuring their volume. Knowing weight of PCL and nHA and measuring their real volume by using pycnometer, their densities can be found. After calibration of the device, PCL and nHA were put into 3.5 cm^3 cylinder chamber. Then measurement was performed for 5 cycle and 5 purges. Average real volume of PCL and nHA was recorded to compute the mean density. Real density of

samples was calculated by taking ratio of measured weight to computed volume (width x thickness x height). Porosity calculation was calculated by following formulae.

$$\rho_{theoretical} = x_{HA} * \rho_{HA} + x_{PCL} * \rho_{PCL}$$

$$\rho_{specimen} = \frac{measured\ weight\ (g)}{computed\ volume\ (cm^3)}$$

$$p = 1 - \frac{\rho_{specimen}}{\rho_{theoretical}}$$

Where x_{HA}, x_{PCL} and ρ_{HA}, ρ_{PCL} are weight fractions and density of nHA and PCL, respectively and p is the real porosity of the specimen.

4.4.4. Scanning Electron Microscopy with EDS

Top surface and cross-sectional porosity of film scaffolds and 3D scaffolds were analyzed by Scanning Electron Microscopy (SEM). Field emission SEM, Zeiss, Leo Supra VP 35 model was used. For cross sectional images, specimens were exposed to liquid nitrogen and then immediately cut by pliers. Specimens were sputtered by gold-palladium with Denton vacuum sputtering equipment for 135 seconds. Working distance and the acceleration voltage were 12-15 mm, and 4 kV, respectively. Presence and density of nHA was evaluated by SEM with EDS. EDS analysis was performed to quantify presence of nHA by looking for calcium and phosphate peaks.

4.4.5. Mechanical Properties Evaluation

Tension test of specimens was conducted with Zwick/Roell Universal Testing Machine (Ulm, Germany) device. Specimens were uniaxially elongated with cross head speed of 2 mm/min using 200 N pneumatic load head. During the test, tensile stress versus elongation was recorded.

4.4.6. Viscosity Analysis

The viscosity of pure PCL solution, 10% nHA/PCL solution and 20% nHA/PCL solution were tested via MCR 302 Rheometer (Anton Paar, Graz, Austria) in order to understand the relationship between porosity and viscosity and solution behavior under shear. A parallel plate head with 0.5 mm of gap was selected for all samples. Frequency sweep test and complex viscosity measurement tests were carried out. In the frequency sweep test,

the strain amplitude was set to 1%. The low and high angular frequencies were set to 0.1 Hz and 100 Hz at the room temperature (25 $^{\circ}$C), respectively.

4.4.7. Contact Angle Measurement

Water contact angle measurement was performed to analyze surface properties of fabricated scaffolds having various nHA content (0, 10, 20% w/w) and scaffolds coated with p(HEMA-*co*-EGDMA) via iCVD. About 5 µl of distilled water was dropped onto flat samples and measurement was recorded. Three measurements were conducted for average contact angles of each set of samples.

4.4.8. Ellipsometer and FTIR

The thickness of the deposited p(HEMA-*co*-EGDMA) films on the Si wafer were measured by M2000D J.A. Woollam Co Inc. ellipsometer (Lincoln, Nebraska, U.S.) Main measurement principle is based on the reflection of the polarized light from the deposited polymeric films with a difference in amplitude and angle. By using the detector and this change, thickness is determined. During the measurements, an 65° alignment angle, scanned angles from 65° to 75° with 5° increments and 315-718 nm wavelength range were applied. Cauchy model was used to fit data onto the Si wafer with native oxide.

FTIR was used to validate the successful deposition using iCVD. Si wafer which has been deposited via iCVD was used as the sample to investigate the chemical composition of a polymeric thin film. Bare Si wafer spectra was then subtracted from the data as background subtraction to get only the deposited p(HEMA-*co*-EGDMA) spectra. Thermo-Fisher Scientific, Nicolet Is10 FTIR equipment was utilized for characterization purposes. Data were collected within the wavelength range of 800-4000 cm^{-1} with the resolution of 4 cm^{-1} over 62 scans. FTIR measurements were performed in nitrogen atmosphere to obtain a smoother spectrum.

Chapter 5

Results and Discussion

In this chapter, characterization results of the fabricated film and 3D scaffolds are presented. Specifically, BMD and an in-depth analysis of the porosity using both micro-CT and gas pycnometer is presented first. The micro-CT analysis includes the evaluation of pore shape morphology and distribution, anisotropy of pore network evaluation, pore size distribution and overall porosity quantification. Porosity is also characterized next using SEM with EDS for both film and 3D scaffolds for surface and cross-sectional observations. UTM test results are presented in the following section for fabricated film substrates. Viscosity of the NIPS based slurries for different percentage of nHA content are also measured and discussed here. Finally contact angle measurements and ellipsometer and FTIR results are presented for film scaffolds coated with iCVD.

5.1. Bone Mineral Density Analysis

Bone mineral density which is the indication of the amount of mineral available in the bone was evaluated using micro-CT based on detection of the HA amount that exists in the scaffolds. Comparison of the experimental amount used of nHA which was added into the polymer solution when preparing each solution using NIPS with the calculated percentage value of nHA in the scaffolds using micro-CT per calibration procedure with available phantoms is given in Table 6 and Figure 1. Results in Table 6 and Figure 13 reveal that calculated and experimentally used percentage of nHA are following an increasing trend as expected with relatively close values to each other. Discrepancy slightly increases with increasing nHA content but is still in acceptable agreement considering the nano-scale particle size of the nHA content, VOI selection, thresholding, and phantom size and calibration conditions and settings.

Table 6. Bone mineral density (g/cm^3) with respect to PCL and nHA content (%w-%w).

Type of Measurement	10 - 0	10-10	10-20
Micro-CT	0.05 ± 0.005	0.21 ± 0.016	0.43 ± 0.018
Experimental	0	0.28	0.53

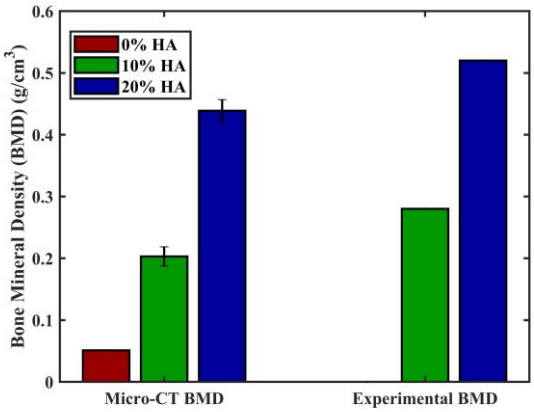

Figure 13. Comparison of bone mineral density (BMD) values obtained using micro-CT analysis and experimental weight percentage.

5.2. Pore Analysis with Micro-CT

In this section we present micro-CT analysis results for both the films scaffolds followed by the pore analysis for 3D scaffold. It is noted that the film analysis includes a comparison based on the nHA content, PCL concentration and thickness whereas the 3D scaffold is carried out for a set nHA content ratio of 12.5.

5.2.1. Pore Analysis of Film Scaffolds

5.2.1.1. Anisotropy of Pore Network

3D model of pore network, as shown by the representative image for a sample film in Figure 14, micro-CT reconstructed images in Figure 15, and degree of anisotropy (DA) in Table 7 showed that pore network orientation were governed by phase separation which occurs at the z-direction from bottom to top of the specimen as shown in Figure 15. Similar to this observation, in the study of Mathieu et al. [63]**,** pores were oriented along the foaming direction by gas foaming technique and showed anisotropic behavior. DA result demonstrated that both neat (pure polymer) and composite (polymer with ceramic) scaffolds exhibited anisotropy (>1) in pore network morphology. However, pore network of composite specimens showed higher anisotropic behavior in comparison with neat

specimen. Adding nHA increases anisotropy and stimulates pore orientation to be in the direction of phase separation. Degree of anisotropy of trabecular bone as the results show in Table 7 are between 1.37-1.53 and agree with the cited range of 1.1 to 2.38 [64], [65] in literature for the characteristic DA of trabecular bone.

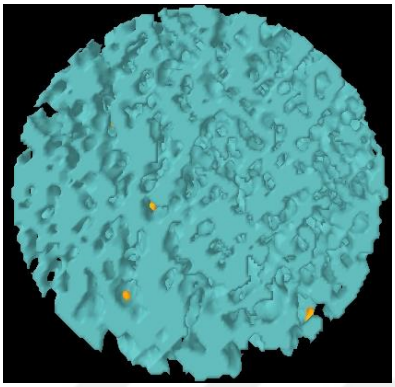

Figure 14. 3D model of interconnected pore network.

5.2.1.2.Pore Shape Morphology and Distribution

Micro CT reconstructed images (Figure 15 and Figure 16) demonstrated that scaffolds have higher porosity and larger pore size near the top/open surface due to higher interaction and mutual affinity between solvent and non-solvent. Because, near the top surface constitutes a polymer-poor phase (i.e. polymer concentration is low) in these areas the phase exchange process is enhanced. Resulting images showed that scaffolds exhibit finger-like interconnected macro void morphology and thin porous surface attributed to instantaneous demixing. Macro voids and pore size becomes smaller as moving towards the bottom of surface which is a polymer-rich phase (i.e. polymer concentration is high). Micro-CT images also showed that pores are oriented along the phase separation direction which occurs from bottom to the top of the scaffold. Figure 16 also shows that larger pores are induced when the PCL concentration is lower for film scaffolds with same amount of nHA content.

Table 7. Degree of Anisotropy of Pore Network of PCL-nHA Scaffolds

PCL - HA content (%w - %w)		
10-0	10-10	10-20
1.37 ± 0.01	1.42 ± 0.01	1.53 ± 0.005

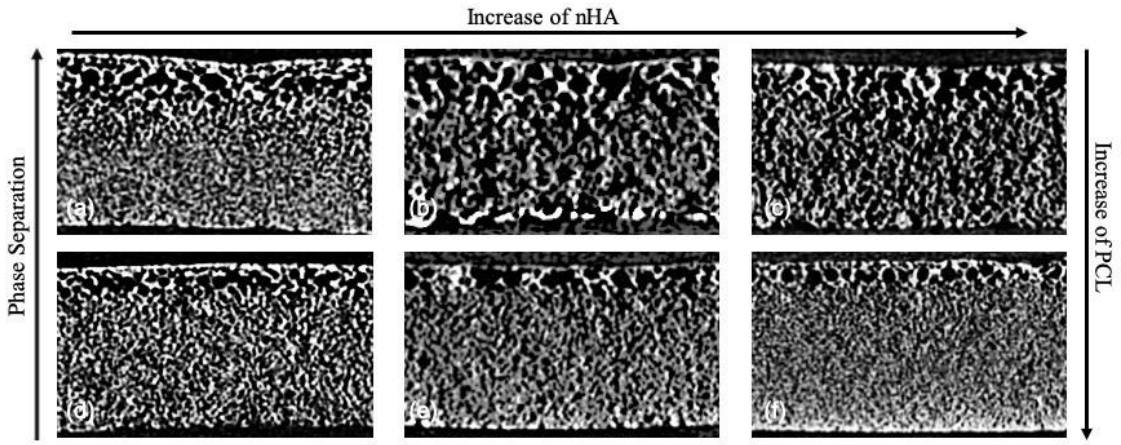

Figure 15. Micro-CT reconstructed images of 10% (top) and 12.5% (bottom) PCL scaffolds with following nHA (w/w) 0% (a and d), 10% (b and e), 20% (c and f)

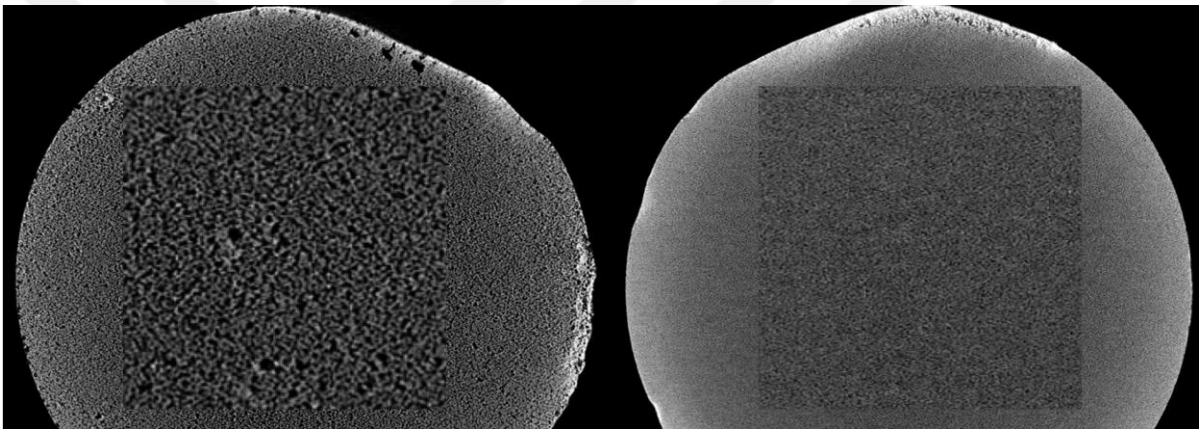

Figure 16. Micro-CT reconstructed images coronal cross section (the direction from surface to bottom) of 10% PCL with 20% nHA (left) and 12.5% PCL scaffolds with %20 nHA (right).

5.2.1.3.Pore Size Distribution

In this section the pore size and its distribution are calculated for film substrates produced using two different weight percentage of PCL content (10% and 12.5%) and three different nHA content (0%, 10%, 20%) and two different thicknesses. Results are presented for the effect of each of the three parameters and are shown altogether in Figure 17 for comparison purposes.

Thickness Effect

As the thickness of scaffolds increases; for all samples (10% PCL and 12.5 % PCL scaffolds), pore size increases and larger pores are induced. Specifically, 10% PCL

scaffolds with 10% and 0% nHA do not have pores in size larger than 142.48 microns but when the thickness increased twofold, scaffolds begin to exhibit pores larger than 142.48 microns in size. In addition, percentage of pores beyond 64.76 microns in size increases from about 24% to 35% for scaffolds containing 20% nHA. Similar results are observed for 12.5% PCL scaffolds as well. When the scaffold thickness is doubled, larger pores are observed with sizes larger than 142.48 microns. One major reason of this increase may be that as thickness increases the pores are being scaled-up and the interaction between solvent and nonsolvent also increases giving rise to a higher amount of solvent upcoming with the deposited solution in the phase separation process.

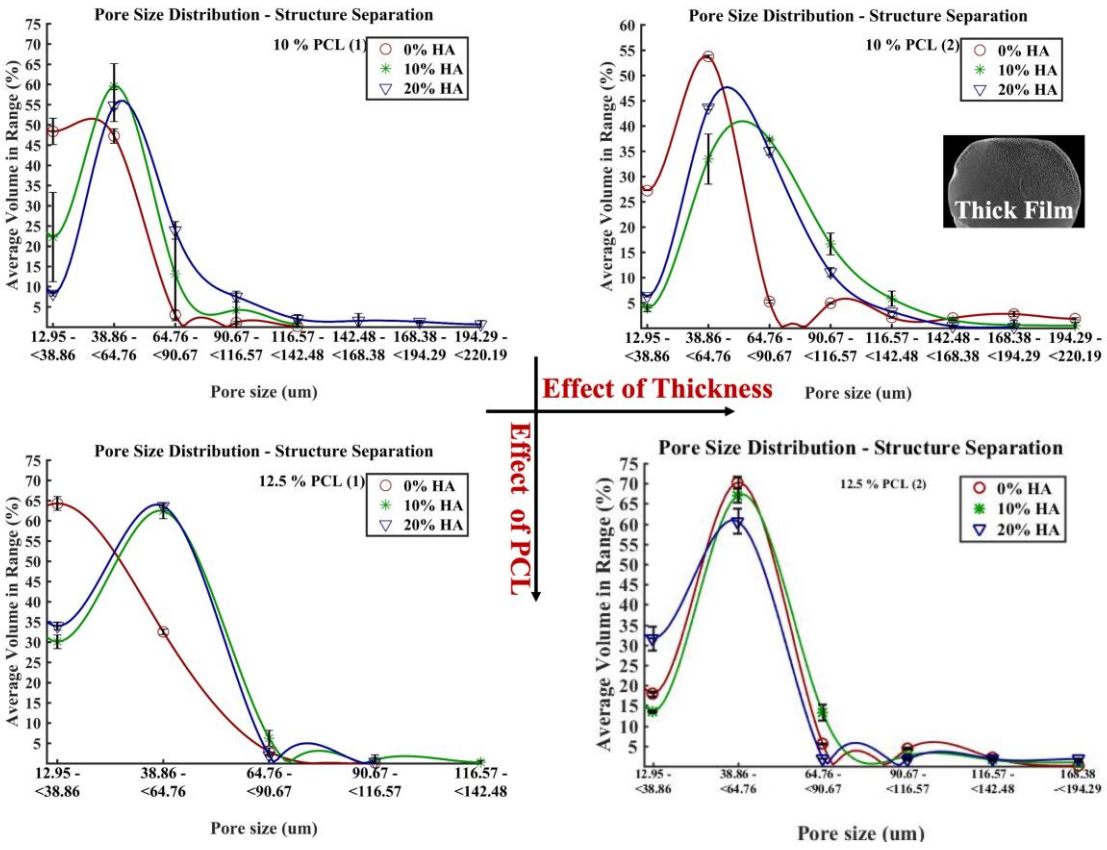

Figure 17. Average volume in the range of different pore size of 10% PCL and 12.5% PCL scaffolds with various HA content. 10% PCL with 0, 10, 20 % nHA scaffolds having a) initial and b) double thickness, 12.5% PCL with 0, 10, 20 % nHA scaffolds having c) initial and d) double thickness.

Effect of nHA content

As the graphs show, presence of nHA in 10% PCL scaffolds significantly increases pore size compared to neat scaffolds. More specifically, for 10% PCL scaffolds, as the content of nHA increases from 0% to 20%, pore size increases. In addition, larger new pores are induced. However, for film scaffolds with double thickness, percentage of pore size larger

than 64.76 microns decreases as the content of nHA increases from 10% to 20% for both PCL concentrations (10% and 12.5%). But, independently from the nHA content, presence of nHA still induces larger pores in size when compared with neat scaffolds.

For the film scaffolds with 12.5 % PCL, as expected, incorporation of nHA increases pore size and induces larger pores compared to neat PCL scaffolds. However, for scaffolds with a single thickness, percentage of pores larger than 64 microns in size decreases with increase of nHA content from 10% to 20%. Hence, it can be concluded that film scaffolds with both 12.5% and 10% PCL content and single and double thickness exhibit overall similar behavior in terms of their pore size characteristics.

Effect of PCL concentration

From a broader perspective, it can be stated that pore size decreases with increase of PCL concentration as shown in the pore size distribution graphs in Figure 17. When the scaffolds with the same thickness and nHA ratios are compared with each other, *as the scaffold PCL concentration increases from 10% to 12.5%*, the following are observed: 1) summation of percentage of pores between 12.95 and 38.86 (first interval of pore size) and pores between 38.86 and 64.76 (second interval of pore size) always increases as shown in Table 10-13. 2) while pores larger than 142.48 microns in size were observed within 10% PCL scaffolds with various nHA content, these did not exist for 12.5% PCL scaffolds having various nHA content (0, 10, 20% w/w).

*With respect to the effect of the nHA content***,** for film scaffolds containing 10% and 20% nHA, the following observations can be made: 1) pores with size larger than 64.76 microns decreases and 2) larger pores with size exceeding 90.67 microns almost entirely disappear. Based on the average size of pores indicated in these two ranges, it can be concluded that larger pores with size larger than 64.76 microns shrink to smaller size pores and hence contributes to the percentage increase of smaller pores especially in the range of 25.95 and 38.86 microns. However, *for the neat scaffolds*, it is observed that percentage of pores larger than 64.76 microns does not change significantly; instead pores in the range of 38.86 and 64.66 microns decreases and these are the dominant contributors for the percentage increase of the smallest pore size. To sum up, as the PCL concentration increases, pore size decreases and results in dominance of smaller pores in size because of higher concentration of PCL. Also, pore size distribution graph shifts to the right reflecting the tendency towards smaller pore size inclusions.

5.2.1.4. Overall Porosity

From the micro-CT overall porosity results, the graphs on the left of Figure 18 demonstrate that as *the concentration of PCL* increases in the solution, percentage of overall porosity of the fabricated scaffolds decreases with the same amount of nHA content for the initial single thickness film scaffolds. More specifically, film scaffolds with 12.5% PCL concentration for various nHA contents (0%, 10% and 20%) have lower porosity than scaffolds with 10% PCL concentration for the corresponding nHA contents due to the higher polymer concentration. However, 10% and 12.5% PCL solution, as expected it is observed that the overall porosity of scaffolds increased with the addition of nHA content More specifically in this study, according to Figure 18, film scaffolds with 10% PCL shows continuous overall porosity increase as the nHA content increases from 0 to 20% which is consistent with porosity measurement with gas pycnometer. It is important to note that film scaffolds with 10% PCL scaffolds having 10% nHA content exhibit maximum porosity. One possible cause of this outcome might be related to the polymer matrix break-down by nanoparticles that could have resulted in a viscosity reduction. Nevertheless, as the polymer concentration is higher, effect of the incorporation of nHA on the overall porosity diminishes and nHA addition dramatically increases the viscosity after a certain threshold value which resulted in a lower porosity. Specifically, as the concentration of nHA increases from 10% to 20% in film scaffolds with 12.5% PCL concentration and double thickness, overall porosity decreased as a result of exceeding the threshold concentration of nHA. Rheology results showed that although highest viscosity exist in the solution with 20% nHA content, presence of nHA still enhances porosity and pore size. In addition, neat solution has higher viscosity than the solution with 10% nHA content. The results of rheological test support that certain and sufficient number of nanoparticles might create ball bearing effect in the polymer matrices giving rise to a possible in decrease of the viscosity. On the other hand, as *the thickness of scaffolds is increased to a double thickness*, overall porosity of film scaffolds with 10% and 12.5% PCL concentration and for both 0% and 10% nHA content, increases. The reason for this behavior may be that thicker scaffolds require higher amount of the solution for deposition and contain therefore a higher amount of solvent in the ethanol bath. This overall increase may result in the enhancement of the interaction between solvent and non-solvent phases leading to an enhancement in the phase exchange taking place between them. However, it is noted that despite this enhancement, there is

no significant overall porosity difference between scaffolds having different thicknesses based on gas pycnometer porosity calculations. However, in the case of higher nHA content of 20%, it is observed that overall porosity decreases with thickness probably due to presence of high amount of nHA that resulted in overall high concentration of solution used for the film scaffold fabrication.

Table 8. Overall porosity of films scaffolds with 10% PCL concentration and various nHA contents.

10% PCL	**0% HA**		**10% HA**		**20% HA**	
Thickness:	Single	Double	Single	Double	Single	Double
(mm)	0.8-0.9	1.6-1.8	0.8-0.9	1.6-1.8	0.8-0.9	1.6-1.8
Porosity (%)	48.8	52.8	58.4	68.8	61.9	57.3

Table 9. Overall porosity of film scaffolds with 12.5% PCL concentration and various % nHA contents.

12.5% PCL	**0% HA**		**10% HA**		**20% HA**	
Thickness:	Single	Double	Single	Double	Single	Double
(mm)	0.8-0.9	1.6-1.8	0.8-0.9	1.6-1.8	0.8-0.9	1.6-1.8
Porosity (%)	46.8	54.9	41.2	58.8	50.5	44.9

Table 10. Pore size distribution of film scaffolds with 10% PCL concentration and single (initial) thickness. Average pore volume is given in the corresponding size ranges.

Average Volume in Range ± Std (%) for initial thickness[1] of 10% PCL Scaffolds.						
Range (um)	**0% HA**		**10% HA**		**20% HA**	
12.95 - < 38.86	48.4	±3.3	22.3	±11	8.2	±0.4
38.86 - < 64.76	47.3	±1.8	59.6	±5.6	54.8	±3.9
64.76 - < 90.67	3.1	±0.99	13.2	±11.6	23.94	±2.17
90.67 - < 116.57	1.1	±0.39	4.2	+4.2	7.5	±1.3
116.57 - < 142.48	0.24	±0.1	0.8	±0.8	2	±1.1
142.48 - < 168.38	-	-	-	-	1.6	±1.8
168.38 - < 194.29	-	-	-	-	1.3	±0.4
194.29 - < 220.19	-	-	-	-	0.7	+1

Table 11. Pore size distribution of film scaffolds with 10% PCL concentration and doubled thickness. Average pore volume is given in the corresponding size ranges.

Average Volume in Range ± Std (%) for double thickness[2] 10% PCL scaffolds.						
Range (um)	**0% HA**		**10% HA**		**20% HA**	
12.95 - < 38.86	27.2	±0.01	3.9	±0.70	6.3	±0.19
38.86 - < 64.76	53.8	±0.30	33.5	±4.95	43.6	±0.38
64.76 - < 90.67	5.3	±0.31	37.3	±0.27	35	±0.78
90.67 - < 116.57	4.9	±0.17	16.7	±2.17	11.	±0.91
116.57 - < 142.48	2.1	±0.19	5.8	±1.49	3.3	±0.16
142.48 - < 168.38	2	±0.13	1.6	±0.09	0.4	±0.22
168.38 - < 194.29	2.8	±0.52	0.6	±0.90	0.23	±0.12
194.29 - < 220.19	1.9	≠0.21	0.5	±0.71	-	-

Table 12. Pore size distribution of film scaffolds with 12.5% PCL concentration and single (initial) thickness. Average pore volume is given in the corresponding size ranges.

Average Volume in Range ± Std (%) for initial thickness[1] of 12.5% PCL scaffolds.						
Range (um)	**0% HA**		**10% HA**		**20% HA**	
12.95 - < 38.86	64.3	±1.70	30.1	±1.69	34	±0.99
38.86 - < 64.76	32.6	±0.65	62.5	±1.93	64	±0.35
64.76 - < 90.67	3	±0.86	6.2	±1.96	2	±0.25
90.67 - < 116.57	0.2	±0.19	0.9	±1.26	0.4	±0.39
116.57 - <142.48	-	-	0.3	±0.41	-	-
142.48 - < 168.38	-	-	-	-	-	-
168.38 - < 194.29	-	-	-	-	-	-
194.29 - < 220.19	-	-	-	-	-	-

Table 13. Pore size distribution of film scaffolds with 12.5% PCL concentration and doubled thickness. Average pore volume is given in the corresponding size ranges.

Average Volume in Range ± Std (%) for double thickness[2] of 12.5% PCL scaffolds.						
Range (um)	**0% HA**		**10% HA**		**20% HA**	
12.95 - < 38.86	17.8	±0.65	13.5	±0.27	31.5	±3.04
38.86 - < 64.76	70.2	±1.46	67	±1.70	60.6	±3.13
64.76 - < 90.67	5.5	±0.15	13.2	±1.93	1.9	±0.09
90.67 - < 116.57	4.3	±0.21	2.6	±0.22	1.6	±0.20
116.57 - < 142.48	2	±0.36	1.5	±0.03	1.8	±0.22
142.48 - < 168.38	0.1	±0.09	0.9	±0.1	1.8	±0.18
168.38 - < 194.29	-	-	0.8	±0.002	0.7	±0.48
194.29 - < 220.19	-	-	0.2	±0.37	0.1	±0.14

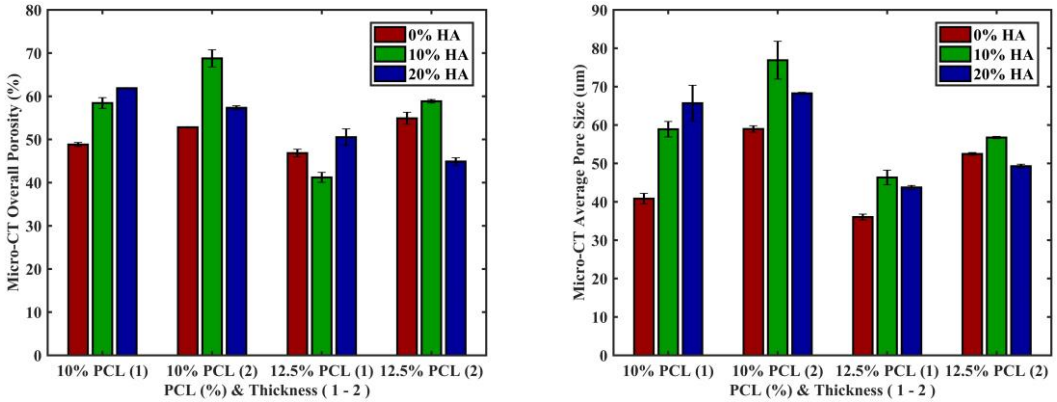

Figure 18. Overall porosity (left) and average pore size (right) for 10% and 12.5% PCL scaffolds with various nHA content (0, 10, 20 % w/w) and single (1) and double (2) thickness (left).

5.2.2. Pore Analysis of 3D scaffolds

Similar to the in-depth pore size and distribution analysis of film scaffolds, structural morphology of printed PCL-nHA composite 3D scaffold was evaluated using micro-CT. It is observed that the printing was successful as demonstrated in Figure 20 where well-controlled struts and macro channels are clearly obtained (Figure 20). Nearly uniformly distributed nHA particles can also be seen in the form of white dots in both the cross-sectional and surface slice images of Figure 20 and Figure 21. Pore size distribution varies with peak average volume of pores within the range of 6.80 – 8.74 microns (Figure 19).

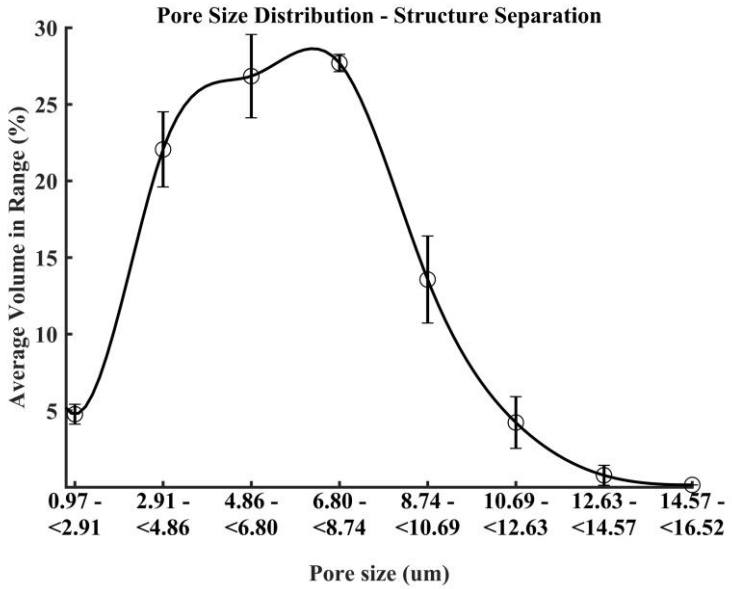

Figure 19. Pore size distribution of trial 3D scaffolds. Percentage of average volume in the range versus range of pore size.

Table 14. Average porosity, pore size and degree of anisotropy for 3D PCL-nHA scaffold

Overall Porosity (%)	Pore Size (um)	Degree of Anisotropy
52.8 ± 2.85	6.6 ± 0.3	1.36 ± 0.12

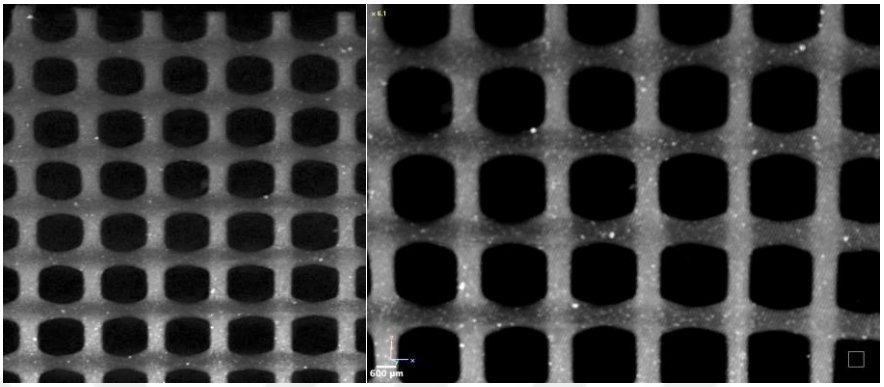

Figure 20. Micro-CT images of 3D PCL-nHA scaffold.

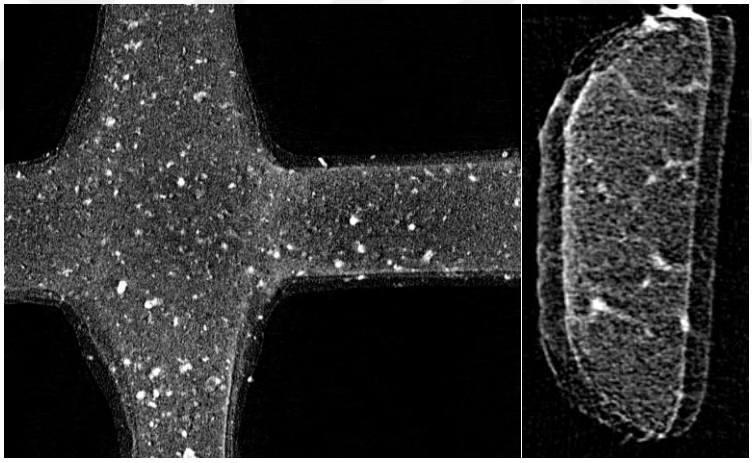

Figure 21. Micro-CT images of 3D PCL-nHA scaffolds surface slice section (left) and internal cross section (right).

5.3. Porosity Evaluation with Gas Pycnometer

Based on porosity evaluation using gas pycnometer for the film scaffolds, there seems to be no significant variation between these film scaffolds with varying polymer concentrations nor thickness. However, overall porosity is observed to slightly increase for film scaffolds with the increase of nHA which is in agreement with the results obtained using micro-CT images and analysis presented in section 5.2.1.4.

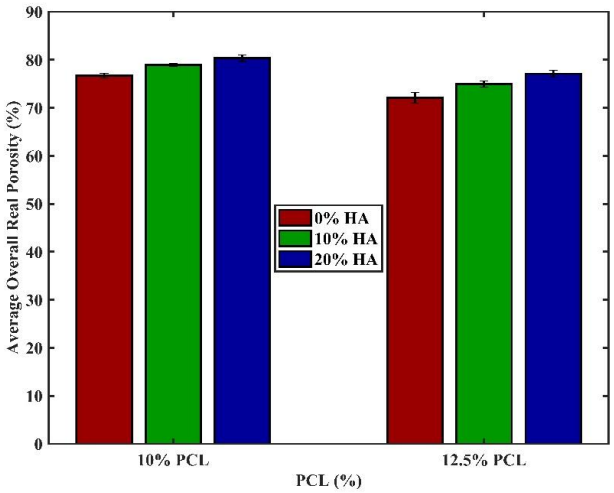

Figure 22. Overall average porosity results.

5.4.Scanning Electron Microscopy Analysis with EDS

5.4.1. SEM Analysis of Film Scaffolds

SEM characterization results (Figure 23) demonstrated that macro voids were present with honeycomb shaped pore morphology and were distributed uniformly throughout the cross section for all film scaffolds with various nHA contents (0%, 10%, 20% (w/w)). However, film scaffolds with 10% and 20% nHA content displayed larger pores in diameter at their cross section (Figure 25). This result is consistent with the structure separation (pore size) distribution results obtained earlier using micro-CT and CTan software (Figure 17 and Figure 18 (right)). Moreover, images of the top surfaces of film scaffolds showed that all specimens exhibited surface porosity. However, neat scaffolds displayed more uniform surface porosity than scaffolds containing nHA nanoparticles. On the other hand, PCL/nHA scaffolds displayed a larger pore size on the top of the surfaces than those of pure PCL scaffolds. For the composition evaluation, EDS analysis was performed. Calcium and phosphate peaks as expected are clearly visible as shown in the EDS graph (Figure 22 (right)).

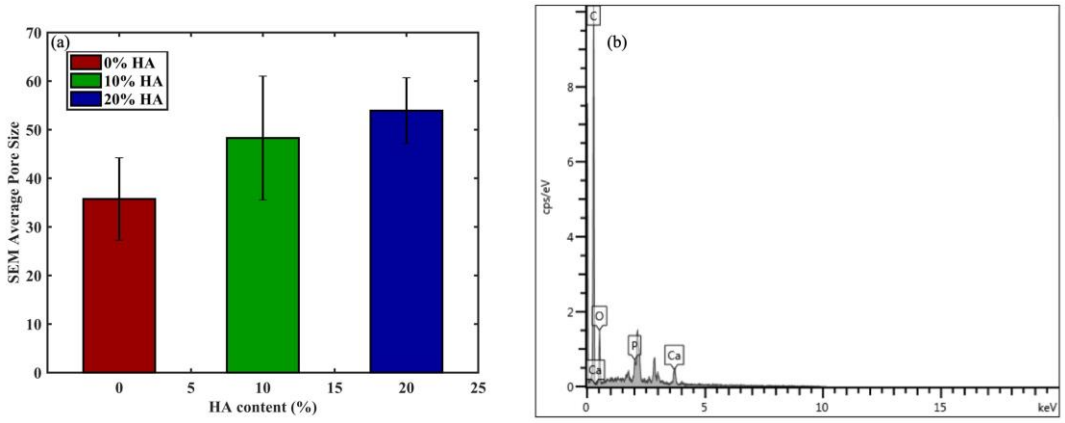

Figure 23. FE-SEM result (left) and EDS analysis (right) of cross-sectional average pore size of film scaffolds with 10% PCL concentration and various nHA content.

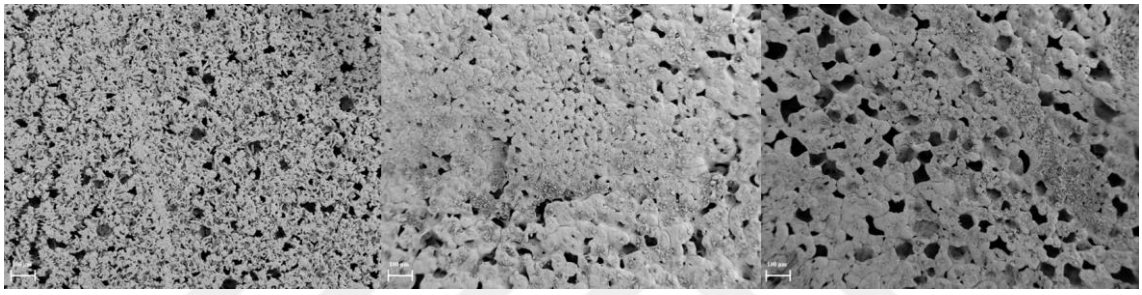

Figure 24. FE-SEM top surface images of film scaffolds with 0% PCL concentration and from left to right with 0%, 10%, 20% nHA (w/w).

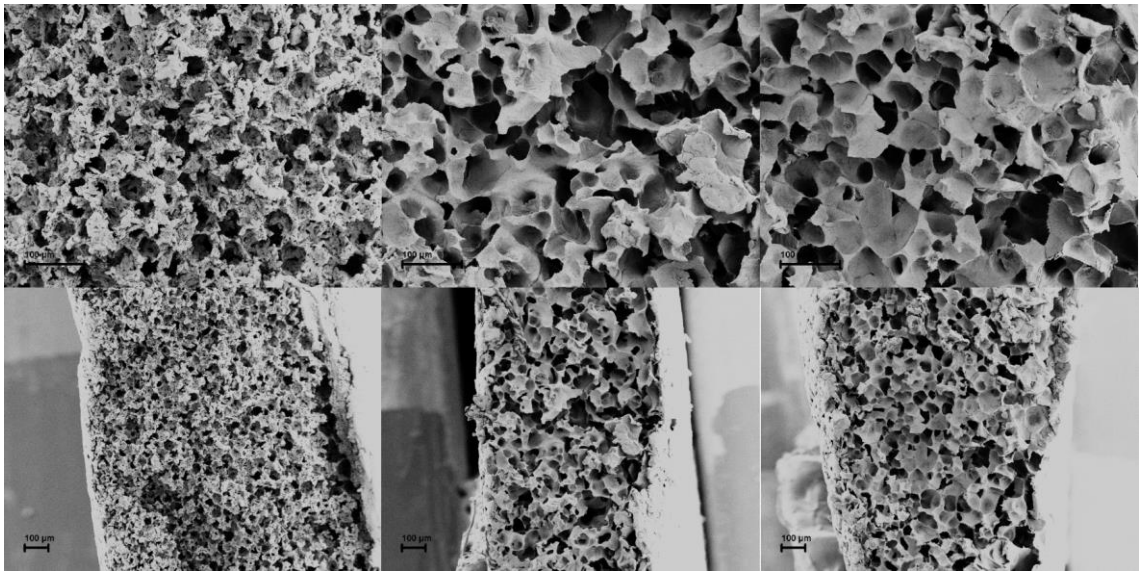

Figure 25. FE-SEM cross section images of film scaffolds with 10% PCL concentration and from left to right with 0%, 10%, 20% nHA (w/w).

5.4.2. SEM analysis of 3D scaffold

Surface and cross section porosity characteristics was also analyzed for the fabricated 3D scaffold using FE-SEM. Obtained results are shown in Figure 26 which demonstrate that struts of the 3D scaffold exhibit porous morphology with an average pore size of 6-7 microns confirming the results for the average pore size obtained using micro-CT and CTAn software presented earlier (Figure 19).

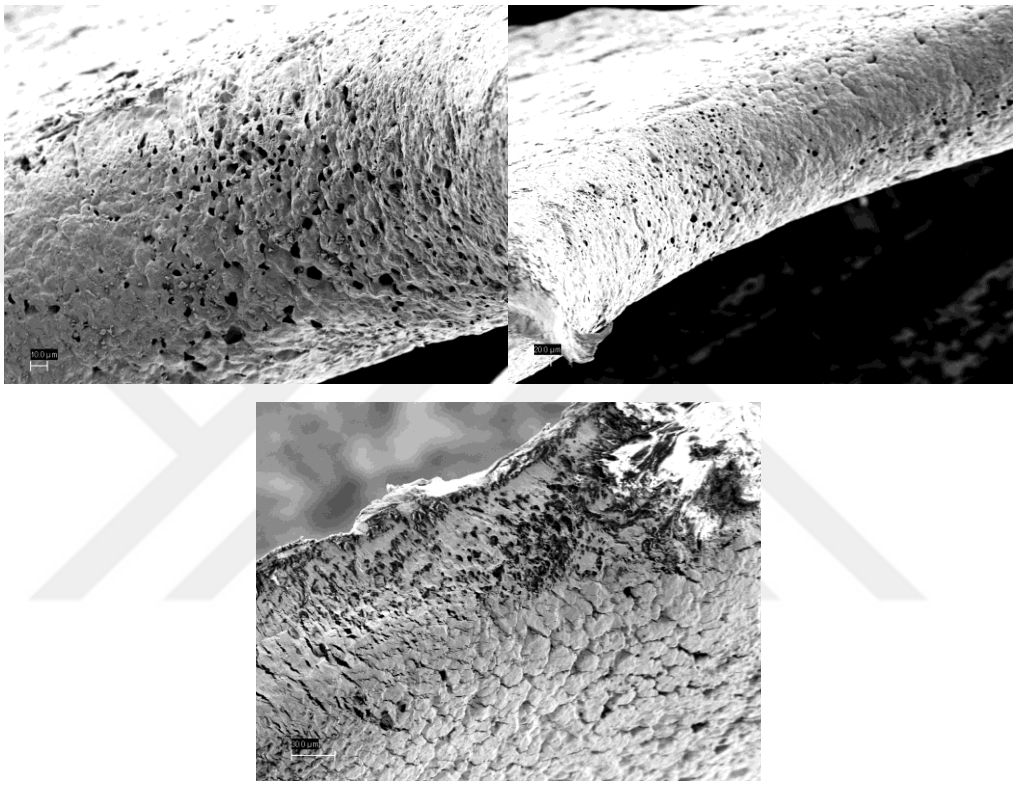

Figure 26. FE-SEM images of 3D PCL-nHA scaffolds.

5.5. Mechanical Properties

Tension tests using UTM as shown in Figure 27 demonstrated that the mechanical strength of fabricated film scaffolds show an increasing trend up to a certain value with the increase of nHA content. More specifically, addition of nHA resulted in an increase of both the ultimate tensile strength and Young's modulus of scaffolds up to 10% nHA content but showed a decrease for the highest nHA content of 20%. Film scaffolds with 10% PCL concentration and 10% nHA content exhibited the highest Young's modulus of (15.7 ± 0.42 MPa) as shown in Figure 27 (right) whereas scaffolds with 20% nHA content displayed a higher elongation and toughness in comparison to neat film scaffolds and scaffolds with 10% nHA content. However, ultimate tensile stress and modulus of

elasticity slightly decreases when the nHA content is 20%. It can be said that 10% nHA content is the threshold for enhancing the mechanical performance and mechanical test results showed that incorporation of nHA into PCL matrices overall enhances mechanical properties of scaffolds.

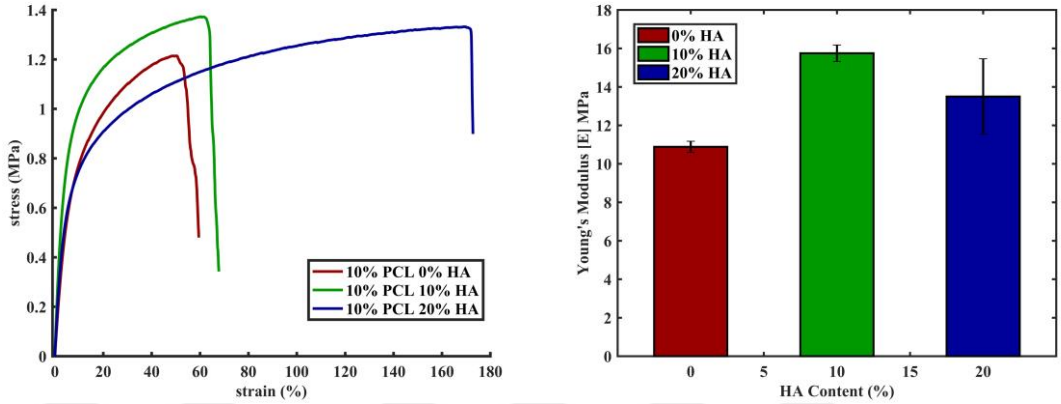

Figure 27. Mechanical tests of 10% PCL scaffolds with 0, 10, 20% nHA: tensile stress versus strain response (left), Young's modulus (right).

5.6. Viscosity Analysis

Viscosity analysis of solutions with various nHA concentrations (0%, 10%, 20% w/w) showed different rheological behavior with respect to their nHA content as shown in Figure 26. As expected, the solution with 20% nHA content demonstrated the highest complex and shear viscosity based on frequency sweep test due its highest concentration content (Figure 28). Nonetheless, the solution containing 10% nHA displayed a lower viscosity than pure PCL solution. The reason is attributed to the ball bearing effect created by the nHA particles entering polymer matrix. However, when the nHA concentration increases from 10% to 20% by exceeding the threshold amount of nHA, viscosity is observed to increase. Lower viscosity might be attributed to the cause of higher porosity observed in the fabricated film scaffolds (Figure 28) using this solution with 10% nHA content.

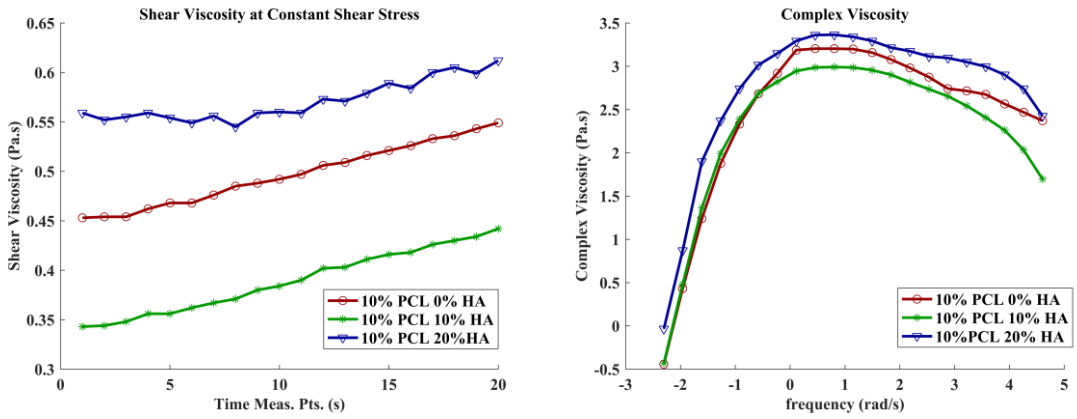

Figure 28. Rheological analysis of 10% PCL solution with various nHA content. Shear viscosity at constant shear stress versus time elapsed (left) and complex viscosity versus frequency (right).

5.7. Contact Angle Measurement

Water contact angle measurement were carried out for the film scaffolds with single thickness 10% PCL with various nHA content (0, 10, 20% w/w) in their uncoated and coated forms. Results shown in Figure 29 demonstrated that while scaffold coated with p(HEMA-*co*-EGDMA) exhibit hydrophilic surface apparent with a contact angle measurement below 90º, non-coated scaffolds with various nHA content displayed contact angle measurements consistent with a hydrophobic surface. Moreover, as the content of nHA increases, contact angle and hence surface hydrophobicity decreases, i.e. hydrophilicity increases.

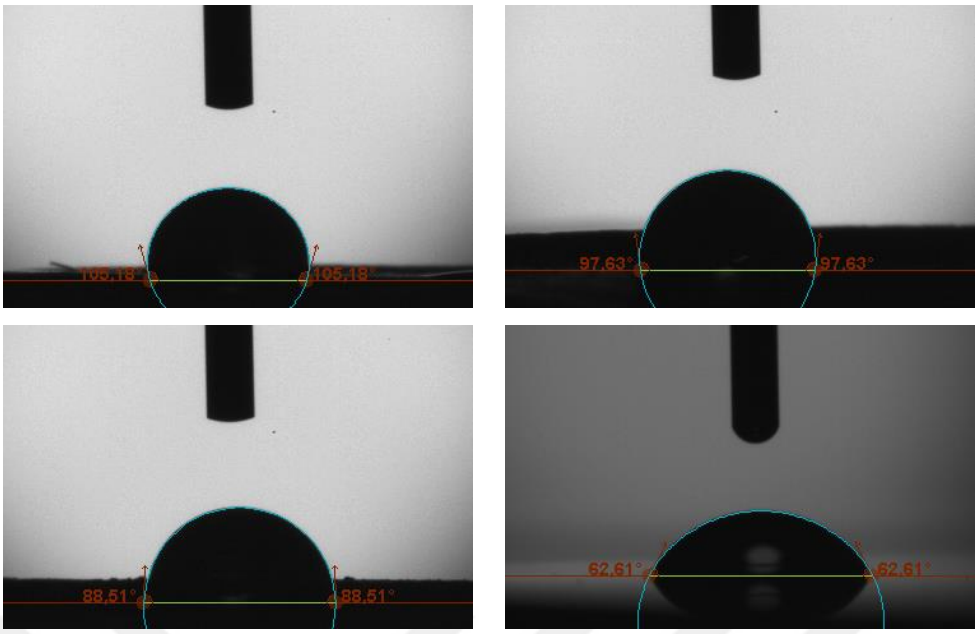

Figure 29. Contact angle measurement of coated and uncoated film scaffolds with 10% PCL, with 0% nHA (top first), 10% nHA (top second), 20% nHA (bottom third for single thickness.

Table 15. Water contact angle measurement of coated and uncoated 10% PCL film scaffolds with various nHA content (0, 10, 20% w/w) and PCL for single thickness.

0% HA	**10% HA**	**20% HA**	**Coating**
103.9° ± 2.5	99.5º ± 2.6	95.7º ± 3.2	62.1º ± 0.6

5.8. Ellipsometer and FTIR

The thickness of p(HEMA-*co*-EGDMA) deposition on the Si wafer used for the coated sample was measured as 284±1 nm with the mean square error of 8.75. FTIR spectra confirms the p(HEMA-*co*-EGDMA) deposition was achieved successfully by the appearance of three main peaks in the spectra measurement. The absorption band at 1733 cm^{-1} corresponds to C=O stretching with high intensity. The peak at 2962 cm^{-1} belongs to O-H stretching and the peak at 1260 cm^{-1} corresponds to the C-O stretching and vibrational mode [66] [67]

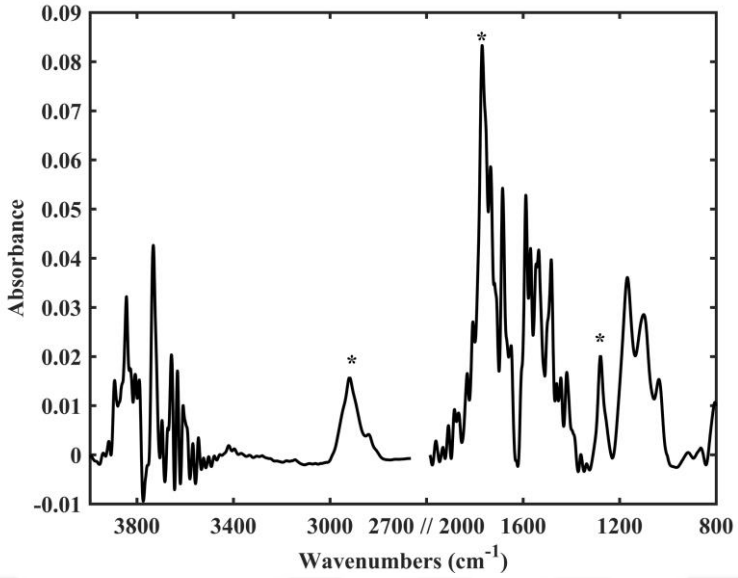

Figure 30. FTIR spectra of deposited p(HEMA-co-EGDMA)

Chapter 6

Conclusion and Future Work

6.1. Conclusion

In this thesis PCL-nHA composite porous scaffolds having various nHA content (0, 10, 20% w/w) were successfully fabricated based on non-solvent induced phase separation technique providing multiscale porosity within scaffolds in bone tissue engineering.

The resulting scaffolds were mainly film scaffolds produced with different PCL, nHA content and two different thicknesses as well as a 3D scaffold printed using the NIPS based slurry. All of the resulting film and 3D scaffolds were characterized in terms of pore morphology, size and distribution using an in-depth micro-CT analysis, SEM and UTM analysis. Also, film scaffolds were coated with iCVD and these were characterized using ellipsometer, FTIR and contact angle measurement studies.

The NIPS based slurry preparation process was conducted with 10% and 12.5% PCL/THF (w/v) solution at 40 °C. First, PCL pellets were added gradually into THF solvent. After 24 hours of magnetic stirring, PCL was completely dissolved, and the solution turned into a transparent color. Then, nHA was put into the solution (0%, 10%, 20% w/w). Again, the solution was stirred for 24 hours to get a homogenous slurry. After solution preparation, film scaffolds and 3D scaffold were fabricated.

Effect of PCL concentration, nHA content and scaffold thickness were investigated next with respect to scaffold porosity and morphology. For surface functionalization, the scaffolds were coated with p(HEMA-*co*-EGDMA) via iCVD to increase surface hydrophilicity which improves cell adhesion. Characterization studies demonstrated the following results:

1) As the thickness of scaffolds increases; for all samples (10% PCL and 12.5 % PCL scaffolds), pore size increases and larger pores are induced.

2) Presence of nHA generally increases pore size when compared to neat scaffolds.
3) From a broader perspective, pore size decreases with increase of PCL concentration as shown in pore size distribution graphs.
4) Micro-CT overall porosity results showed that as the concentration of PCL increases in the solution, percentage of overall porosity of the fabricated scaffolds decreases among those scaffolds including same amount of nHA and when the initial thickness is fixed.
5) Addition of nHA nanoparticles into polymer solution generally increases the overall porosity among the scaffolds having same polymer concentration and thickness. When the thickness of scaffolds is doubled, overall porosity of 10% and 12.5% PCL scaffolds including 0% and 10% nHA increases.
6) Micro CT images demonstrated that scaffolds have higher porosity and larger pores in size near the top/open surface due to higher interaction and mutual affinity between solvent and non-solvent.
7) 3D model of pore network, micro-CT reconstructed images and degree of anisotropy (DA) results showed that pore network orientation was governed by phase separation which occurs in the z-direction from the bottom to the top of the specimen.
8) SEM results demonstrated that pore morphology was consistent with honeycomb shaped macroviods and was distributed uniformly throughout the cross section for all specimens having various nHA contents (0%, 10%, 20% (w/w)). In addition, surface porosity was observed for both film scaffolds and scaffolds produced by 3D printer.
9) UTM tests demonstrated that mechanical strength of fabricated scaffolds increases with increase of content of nHA. Addition of nHA increases ultimate tensile stress and toughness of materials. 10% PCL scaffolds with 10% nHA exhibit highest Young's modulus.
10) Ellipsometer, FTIR and contact angle showed that film scaffolds were coated successfully via iCVD and hydrophilic surfaces were obtained.

6.2. Future Work

In the near future, 3D scaffolds should be analyzed in more detail similar to the extensive analysis to the film substrates using NIPS. Specifically, 3D scaffolds with various nHA (0, 10, 20%) content should be fabricated and characterization studies including porosity using micro-CT and SEM, UTM can be performed. Similar to the film scaffolds, 3D scaffolds could be coated with iCVD and their characterizations could be performed. Their morphological, structural, mechanical properties need to be evaluated as was done in this thesis for film scaffolds. 3D scaffolds coated with p(HEMA-*co*-EGDMA) via iCVD for surface functionalization could be further characterized to validate the resulting enhancement in biological activities. For that purpose, a comparative analysis based on in-vitro tests can be performed for all coated and non-coated samples. The major motivation behind all these suggested future work and similar add-on work is that surface functionalization and structural 3D composition do affect biological activities in terms of cell attachment, proliferation and differentiation.

Bibliography

[1] M. S. Ghiasi, J. Chen, A. Vaziri, E. K. Rodriguez, and A. Nazarian, 'Bone fracture healing in mechanobiological modeling: A review of principles and methods', *Bone Reports*, vol. 6, pp. 87–100, 2017.

[2] P. A. Gunatillake, R. Adhikari, and N. Gadegaard, 'Biodegradable synthetic polymers for tissue engineering', *Eur. Cells Mater.*, vol. 5, pp. 1–16, 2003.

[3] Y. Kuboki *et al.*, 'BMP-induced osteogenesis on the surface of hydroxyapatite with geometrically feasible and nonfeasible structures: topology of osteogenesis', *J. Biomed. Mater. Res. An Off. J. Soc. Biomater. Japanese Soc. Biomater. Aust. Soc. Biomater.*, vol. 39, no. 2, pp. 190–199, 1998.

[4] V. Karageorgiou and D. Kaplan, 'Porosity of 3D biomaterial scaffolds and osteogenesis', *Biomaterials*, vol. 26, no. 27, pp. 5474–5491, 2005.

[5] S. F. Hulbert, F. A. Young, R. S. Mathews, J. J. Klawitter, C. D. Talbert, and F. H. Stelling, 'Potential of ceramic materials as permanently implantable skeletal prostheses', *J. Biomed. Mater. Res.*, vol. 4, no. 3, pp. 433–456, 1970.

[6] R. N. Wenzel, 'Surface roughness and contact angle.', *J. Phys. Chem.*, vol. 53, no. 9, pp. 1466–1467, 1949.

[7] H. Yuan, K. Kurashina, J. D. de Bruijn, Y. Li, K. De Groot, and X. Zhang, 'A preliminary study on osteoinduction of two kinds of calcium phosphate ceramics', *Biomaterials*, vol. 20, no. 19, pp. 1799–1806, 1999.

[8] S. J. Hollister, 'Porous scaffold design for tissue engineering', *Nat. Mater.*, vol. 4, no. 7, p. 518, 2005.

[9] S. M. Giannitelli, D. Accoto, M. Trombetta, and A. Rainer, 'Current trends in the design of scaffolds for computer-aided tissue engineering', *Acta Biomater.*, vol. 10, no. 2, pp. 580–594, 2014.

[10] J. Zhao, L. Y. Guo, X. B. Yang, and J. Weng, 'Preparation of bioactive porous HA/PCL composite scaffolds', *Appl. Surf. Sci.*, vol. 255, no. 5 PART 2, pp. 2942–2946, 2008.

[11] B. Chuenjitkuntaworn, W. Inrung, D. Damrongsri, K. Mekaapiruk, P. Supaphol, and P. Pavasant, 'Polycaprolactone/hydroxyapatite composite scaffolds: Preparation, characterization, and in vitro and in vivo biological responses of human primary bone cells', *J. Biomed. Mater. Res. - Part A*, vol. 94, no. 1, pp.

241–251, 2010.

[12] A. Salerno, S. Zeppetelli, E. Di Maio, S. Iannace, and P. A. Netti, ‘Processing/structure/property relationship of multi-scaled PCL and PCL-HA composite scaffolds prepared via gas foaming and NaCl reverse templating’, *Biotechnol. Bioeng.*, vol. 108, no. 4, pp. 963–976, 2011.

[13] S. H. Lee *et al.*, ‘Fabrication of 3D alginate scaffold with interconnected pores using wire-network molding technique’, *Tissue Eng. Regen. Med.*, vol. 10, no. 2, pp. 53–59, 2013.

[14] Y. S. Cho *et al.*, ‘Fabrication of dual-pore scaffolds using SLUP (salt leaching using powder) and WNM (wire-network molding) techniques’, *Mater. Sci. Eng. C*, vol. 45, pp. 546–555, 2014.

[15] D. G. Sohn, M. W. Hong, Y. Y. Kim, and Y. S. Cho, ‘Fabrication of Dual-pore Scaffolds Using a Combination of Wire-Networked Molding (WNM) and Non-solvent Induced Phase Separation (NIPS) Techniques’, *J. Bionic Eng.*, vol. 12, no. 4, pp. 565–574, 2015.

[16] M. I. Hassan, T. Sun, and N. Sultana, ‘Fabrication of Nanohydroxyapatite/Poly(caprolactone) Composite Microfibers Using Electrospinning Technique for Tissue Engineering Applications’, *J. Nanomater.*, vol. 2014, pp. 1–7, 2014.

[17] L. Li, G. Li, J. Jiang, X. Liu, L. Luo, and K. Nan, ‘Electrospun fibrous scaffold of hydroxyapatite/poly (∈-caprolactone) for bone regeneration’, *J. Mater. Sci. Mater. Med.*, vol. 23, no. 2, pp. 547–554, 2012.

[18] I. Rajzer, ‘Fabrication of bioactive polycaprolactone/hydroxyapatite scaffolds with final bilayer nano-/micro-fibrous structures for tissue engineering application’, *J. Mater. Sci.*, vol. 49, no. 16, pp. 5799–5807, 2014.

[19] L. Shor, S. Güçeri, X. Wen, M. Gandhi, and W. Sun, ‘Fabrication of three-dimensional polycaprolactone/hydroxyapatite tissue scaffolds and osteoblast-scaffold interactions in vitro’, *Biomaterials*, vol. 28, no. 35, pp. 5291–5297, 2007.

[20] J. Y. Kim, T. J. Lee, D. W. Cho, and B. S. Kim, ‘Solid free-form fabrication-based PCL/HA scaffolds fabricated with a multi-head deposition system for bone tissue engineering’, *J. Biomater. Sci. Polym. Ed.*, vol. 21, no. 6–7, pp. 951–962, 2010.

[21] S. A. Park, S. H. Lee, and W. D. Kim, ‘Fabrication of porous polycaprolactone/hydroxyapatite (PCL/HA) blend scaffolds using a 3D plotting system for bone tissue engineering’, *Bioprocess Biosyst. Eng.*, vol. 34, no. 4, pp. 505–513, 2011.

[22] P. Coimbra *et al.*, *Characterization of poly (caprolactone)/ hydroxyapatite composite scaffolds produced by a melt extrusion additive manufacturing technique*. 2016.

[23] J. T. Jung, J. F. Kim, H. H. Wang, E. di Nicolo, E. Drioli, and Y. M. Lee, 'Understanding the non-solvent induced phase separation (NIPS) effect during the fabrication of microporous PVDF membranes via thermally induced phase separation (TIPS)', *J. Memb. Sci.*, vol. 514, pp. 250–263, 2016.

[24] G. R. Guillen, Y. Pan, M. Li, and E. M. V. Hoek, 'Preparation and characterization of membranes formed by nonsolvent induced phase separation: A review', *Ind. Eng. Chem. Res.*, vol. 50, no. 7, pp. 3798–3817, 2011.

[25] D. M. Wang and J. Y. Lai, 'Recent advances in preparation and morphology control of polymeric membranes formed by nonsolvent induced phase separation', *Curr. Opin. Chem. Eng.*, vol. 2, no. 2, pp. 229–237, 2013.

[26] J. W. Kim, K. H. Shin, Y. H. Koh, M. J. Hah, J. Moon, and H. E. Kim, 'Production of poly(ε-caprolactone)/hydroxyapatite composite scaffolds with a tailored macro/micro-porous structure, high mechanical properties, and excellent bioactivity', *Materials (Basel).*, vol. 10, no. 10, 2017.

[27] E. Sapountzi *et al.*, 'One-step fabrication of electrospun photo-cross-linkable polymer nanofibers incorporating multiwall carbon nanotubes and enzyme for biosensing', *J. Electrochem. Soc.*, vol. 162, no. 10, pp. B275–B281, 2015.

[28] H. Ayhan, I. Gürhan, and E. Pişkin, 'Attachment of 3T3 and MDBK cells onto poly(EGDMA/HEMA) based microbeads and their biologically modified forms', *Artif. Cells. Blood Substit. Immobil. Biotechnol.*, vol. 28, no. 2, pp. 155–171, 2000.

[29] R. K. Bose and K. K. S. Lau, 'Initiated CVD of poly(2-hydroxyethyl methacrylate) hydrogels: Synthesis, characterization and in-vitro biocompatibility', *Chem. Vap. Depos.*, vol. 15, no. 4–6, pp. 150–155, 2009.

[30] M. F. Passos *et al.*, 'pHEMA hydrogels: Synthesis, kinetics and in vitro tests', *J. Therm. Anal. Calorim.*, vol. 125, no. 1, pp. 361–368, 2016.

[31] E. De Giglio, D. Cafagna, M. M. Giangregorio, M. Domingos, M. Mattioli-Belmonte, and S. Cometa, 'PHEMA-based thin hydrogel films for biomedical applications', *J. Bioact. Compat. Polym.*, vol. 26, no. 4, pp. 420–434, 2011.

[32] M. Ma, Y. Mao, M. Gupta, K. K. Gleason, and G. C. Rutledge, 'Superhydrophobic fabrics produced by electrospinning and chemical vapor deposition', *Macromolecules*, vol. 38, no. 23, pp. 9742–9748, 2005.

[33] C. Cheng and M. Gupta, 'Surface functionalization of 3D-printed plastics via initiated chemical vapor deposition', *Beilstein J. Nanotechnol.*, vol. 8, no. 1, pp. 1629–1636, 2017.

[34] M. Gupta, V. Kapur, N. M. Pinkerton, and K. K. Gleason, 'Initiated Chemical Vapor Deposition (iCVD) of conformal polymeric nanocoatings for the surface modification of high-aspect-ratio pores', *Chem. Mater.*, vol. 20, no. 4, pp. 1646–1651, 2008.

[35] ‘https://www.doitpoms.ac.uk/tlplib/bones/bone_mechanical.php -- Dissemination of IT for the Promotion of Materials Science (DoITPoMS), University of Cambridge.’ .

[36] P. Pivonka and C. R. Dunstan, ‘Role of mathematical modeling in bone fracture healing.’, *Bonekey Rep.*, vol. 1, 2012.

[37] A. Claes, L., Recknagel, S., Ignatius, ‘Fracture healing under healthy and inflammatory conditions.’, *Nat. Rev. Rheumatol.*, vol. 8, no. 3, p. 133, 2012.

[38] B. McKibbin, ‘The biology of fracture healing in long bones.’, *J. Bone Joint Surg. Br.*, vol. 60, no. 2, pp. 150–162, 1978.

[39] D. J. Nagel, T., Kelly, ‘Mechano-regulation of mesenchymal stem cell differentiation and collagen organisation during skeletal tissue repair.’, *Biomech. Model. Mechanobiol.*, vol. 9, no. 3, pp. 359–372, 2010.

[40] T. A. Marsell, R. and Einhorn, ‘The biology of fracture healing.’, *Injury*, vol. 42, no. 6, pp. 551–555, 2011.

[41] T. A. Gerstenfeld, L. C., Alkhiary, Y. M., Krall, E. A., Nicholls, F. H., Stapleton, S. N., Fitch, J. L., Einhorn, ‘Three-dimensional reconstruction of fracture callus morphogenesis.’, *ournal Histochem. Cytochem.*, vol. 54, no. 11, pp. 1215–1228, 2006.

[42] D. G. Schindeler, A., McDonald, M.M., Bokko, P., Little, ‘Bone remodeling during fracture repair: the cellular picture.’, *Semin. Cell Dev. Biol.*, vol. 19, no. 5, pp. 459–466, 2008.

[43] A. Little, D.G., Ramachandran, M., Schindeler, ‘The anabolic and catabolic responses in bone repair.’, . *Bone Jt. Surg.*, vol. 89, no. B, p. 0, 2007.

[44] H. Strathmann and K. Kock, ‘The formation mechanism of phase inversion membranes’, *Desalination*, vol. 21, no. 3, pp. 241–255, 1977.

[45] M. Di Luccio, R. Nobrega, and C. P. Borges, ‘Microporous anisotropic phase inversion membranes from bisphenol-A polycarbonate: study of a ternary system’, *Polymer (Guildf).*, vol. 41, no. 11, pp. 4309–4315, 2000.

[46] R. Matz, ‘The structure of cellulose acetate membranes 1. The development of porous structures in anisotropic membranes’, *Desalination*, vol. 10, no. 1, pp. 1–15, 1972.

[47] M. A. Frommer and D. Lancet, ‘The mechanism of membrane formation: membrane structures and their relation to preparation conditions’, in *Reverse Osmosis Membrane Research*, Springer, 1972, pp. 85–110.

[48] H. Strathmann, K. Kock, P. Amar, and R. W. Baker, ‘The formation mechanism of asymmetric membranes’, *Desalination*, vol. 16, no. 2, pp. 179–203, 1975.

[49] C. A. Smolders, A. J. Reuvers, R. M. Boom, and I. M. Wienk, ‘Microstructures in phase-inversion membranes. Part 1. Formation of macrovoids’, *J. Memb. Sci.*, vol. 73, no. 2–3, pp. 259–275, 1992.

[50] R. M. Boom, I. M. Wienk, T. Van den Boomgaard, and C. A. Smolders, ‘Microstructures in phase inversion membranes. Part 2. The role of a polymeric additive’, *J. Memb. Sci.*, vol. 73, no. 2–3, pp. 277–292, 1992.

[51] A. J. Reuvers, J. W. A. Van den Berg, and Ca. Smolders, ‘Formation of membranes by means of immersion precipitation: Part I. A model to describe mass transfer during immersion precipitation’, *J. Memb. Sci.*, vol. 34, no. 1, pp. 45–65, 1987.

[52] N. Vogrin, Č. Stropnik, V. Musil, and M. Brumen, ‘The wet phase separation: The effect of cast solution thickness on the appearance of macrovoids in the membrane forming ternary cellulose acetate/acetone/water system’, *J. Memb. Sci.*, vol. 207, no. 1, pp. 139–141, 2002.

[53] D. Li, T.-S. Chung, J. Ren, and R. Wang, ‘Thickness Dependence of Macrovoid Evolution in Wet Phase-Inversion Asymmetric Membranes’, *Ind. Eng. Chem. Res.*, vol. 43, no. 6, pp. 1553–1556, 2004.

[54] A. Conesa, T. Gumí, and C. Palet, ‘Membrane thickness and preparation temperature as key parameters for controlling the macrovoid structure of chiral activated membranes (CAM)’, *J. Memb. Sci.*, vol. 287, no. 1, pp. 29–40, 2007.

[55] J. Zhou, J. Ren, L. Lin, and M. Deng, ‘Morphology evolution of thickness-gradient membranes prepared by wet phase-inversion process’, *Sep. Purif. Technol.*, vol. 63, no. 2, pp. 484–486, 2008.

[56] J. Ren, J. Zhou, and M. Deng, ‘Morphology transition of asymmetric flat sheet and thickness-gradient membranes by wet phase-inversion process’, *Desalination*, vol. 253, no. 1–3, pp. 1–8, 2010.

[57] J. Ren, J. Zhou, and M. Deng, ‘Morphology transition of asymmetric polyetherimide flat sheet membranes with different thickness by wet phase-inversion process’, *Sep. Purif. Technol.*, vol. 74, no. 1, pp. 119–129, 2010.

[58] bruker user manual, ‘No Title’.

[59] https://www.microphotonics.com/, ‘No Title’. .

[60] wikipedia, ‘No Title’. .

[61] M. E. Alf *et al.*, ‘Chemical vapor deposition of conformal, functional, and responsive polymer films’, *Adv. Mater.*, vol. 22, no. 18, pp. 1993–2027, 2010.

[62] S. H. Baxamusa, S. G. Im, and K. K. Gleason, ‘Initiated and oxidative chemical vapor deposition: a scalable method for conformal and functional polymer films on real substrates’, *Phys. Chem. Chem. Phys.*, vol. 11, no. 26, pp. 5227–5240, 2009.

[63] L. M. Mathieu, T. L. Mueller, P. E. Bourban, D. P. Pioletti, R. Müller, and J. A. E. Månson, ‘Architecture and properties of anisotropic polymer composite scaffolds for bone tissue engineering’, *Biomaterials*, vol. 27, no. 6, pp. 905–916, 2006.

[64] R. Müller, S. Matter, P. Neuenschwander, U. W. Suter, and P. Rüegsegger, ‘3D Micro-Tomographic imaging and Quantitative Morphometry for the Nondestructive Evaluation of Porous Biomaterials’, *MRS Proc.*, vol. 461, pp. 217–222, 1996.

[65] S. Forman, J. Káš, F. Fini, M. Steinberg, and T. Ruml, ‘The effect of different solvents on the ATP/ADP content and growth properties of HeLa cells’, *J. Biochem. Mol. Toxicol.*, vol. 13, no. 1, pp. 11–15, 1999.

[66] K. Unger, P. Salzmann, C. Masciullo, M. Cecchini, G. Koller, and A. M. Coclite, ‘Novel light-responsive biocompatible hydrogels produced by initiated chemical vapor deposition’, *ACS Appl. Mater. Interfaces*, vol. 9, no. 20, pp. 17408–17416, 2017.

[67] A. Tufani and G. O. Ince, ‘Permeability of small molecules through vapor deposited polymer membranes’, *J. Appl. Polym. Sci.*, vol. 132, no. 34, 2015.